Oxylipin metabolism is controlled by mitochondrial β-oxidation during bacterial inflammation.

Mariya Misheva[1], Konstantinos Kotzamanis[1*], Luke C Davies[1*], Victoria J Tyrrell[1], Patricia R S Rodrigues[1], Gloria A Benavides[2], Christine Hinz[1], Robert C Murphy[3], Paul Kennedy[4], Philip R Taylor[1,5], Marcela Rosas[1], Simon A Jones[1], Sumukh Deshpande[1], Robert Andrews[1], Magdalena A Czubala[1], Mark Gurney[1], Maceler Aldrovandi[1], Sven W Meckelmann[1], Peter Ghazal[1], Victor Darley-Usmar[2], Daniel White[1], and Valerie B O'Donnell[1]

[1]Systems Immunity Research Institute and Division of Infection and Immunity, and School of Medicine, Cardiff University, UK, [2]Department of Pathology, University of Alabama at Birmingham, Birmingham, AL 35294, USA, [3]Department of Pharmacology, University of Colorado Denver, Aurora, CO 80045, USA, [4]Cayman Chemical 1180 E Ellsworth Rd, Ann Arbor, MI 48108, United States, [5]UK Dementia Research Institute at Cardiff, Cardiff University, UK

Address correspondence: Valerie O'Donnell, o-donnellvb@cardiff.ac.uk or Daniel White, WhiteD13@cardiff.ac.uk, Systems Immunity Research Institute, Cardiff University

[*]Both authors contributed equally to the study

Abstract

Oxylipins are potent mediators requiring strict control. How they are removed en masse during infection/inflammation is unknown. Herein, lipopolysaccharide (LPS) dynamically increased their mitochondrial β-oxidation, impacting leukocyte bioactivity. Genetic/pharmacological targeting of CPT1 showed <50 oxylipins were robustly removed by macrophage mitochondria during inflammation *in vitro* and *in vivo*. Stable isotope-lipidomics demonstrated secretion-reuptake recycling for 12-HETE and its intermediate metabolites. Oxylipin β–oxidation was uncoupled from oxidative phosphorylation. Transcriptional interrogation of human neonatal sepsis revealed significant upregulation of many candidates, encoding proteins for mitochondrial uptake and β-oxidation of long-chain fatty acyls (*ACSL1,3,4*, *ACADVL*, *CPT1B, CPT2*, *HADHB)*. *ACSL1/Acsl1* upregulation was a signature in multiple human/murine macrophage datasets. In summary, mitochondrial β-oxidation is a regulatory metabolic checkpoint for oxylipins during infection. This has implications for patients with *CPT1* deficiency, at higher risk of mortality during respiratory infections. We propose that mitochondrial β-oxidation capacity to remove oxylipins during infection may directly influence development of inflammation.

Introduction

Oxygenated polyunsaturated fatty acids (oxylipins), including eicosanoids and prostaglandins, are essential bioactive lipid mediators during inflammation/infection. There are generated by cyclooxygenases (COX), lipoxygenases (LOX) or cytochrome P450s (CYP), expressed in a variety of tissues [1-10]. They signal through binding and activation of G protein-coupled receptors at sub nM concentrations [1, 5-16]. Oxylipins require deactivation, however our understanding of how this is regulated during infection is poor. Systemic pathways for individual oxylipins, including thromboxane, prostacyclin and hydroxyeicosatetraenoic acids (HETEs) were uncovered in healthy humans decades ago [17-20]. There, infusion of exogenous labelled lipids enabled determination of half-life and metabolites, some of which appear immediately, slowly disappearing over several minutes [21]. Urinary metabolite analysis became the gold standard for whole body oxylipin analysis. Separately, peroxisomal β-oxidation of individual eicosanoids was explored using liver microsomes. There, partial β-oxidation revealed truncated products termed dinors (minus 2C) and tetranors (minus 4C). These were identified as stable intermediates in tissue, plasma and urine [21].

Aside from peroxisomes, mitochondria contain fully competent β-oxidation machinery, used for the first steps of FA-dependent energy metabolism, FA oxidation (FAO) [22, 23]. Here, FA are converted to acetyl-CoA which enters the tricarboxylic cycle (TCA) providing substrates for oxidative phosphorylation (OxPhos) [24]. Although mediated by distinct enzymes to peroxisomes, mitochondrial β-oxidation also involves sequential removal of 2-carbon fragments from the carboxyl terminus. More recently, significant interest in how mitochondrial FAO supports immunity has developed, particularly relating to T cells and macrophages[25, 26]. Saturated FA such as palmitate or stearate are considered the main substrates, however oxylipins generated abundantly during inflammation, have not been considered [19]. We recently showed that endogenously-generated platelet oxylipins are removed by carnitine palmitoyltransferase-1 (CPT1), the mitochondrial import protein for FAs [27]. However, it is not known whether mitochondria also remove oxylipins in macrophages, nor how this might be regulated by inflammation/infection, if this impacts lipid signaling, and if it supplies acetyl-CoA to OxPhos. These are important questions, since macrophages generate large amounts of diverse oxylipins during inflammation/infection, as well as

being exposed to them from inflamed stroma. Currently there is significant interest in how mitochondrial respond to inflammation, and their role in immunometabolism[26, 28, 29]. The traditional view is that M1(LPS) mitochondrial OxPhos is shut down in favor of increased glycolysis, along with increased synthesis of FA [30].

In this study, oxylipin uptake into macrophage mitochondria was revealed as a dynamic process stimulated by inflammation (LPS +/- IFNγ) operating independently of OxPhos and reducing extracellular oxylipin secretion. Using 12-HETE and transcriptional data from multiple sources, a metabolic β-oxidation network for the parent and two tetranor metabolites was revealed. Importantly, modulating oxylipin levels was sufficient to impact on their signaling. Thus, we reveal how oxylipins are consumed by macrophage mitochondria, suggesting that targeting this could represent a route to regulate inflammation. Furthermore, oxylipin levels may be impacted if mitochondrial function is compromised during infection, directly contributing to ensuing damaging host inflammatory responses. Our findings also have implications for humans with the rare genetic disorder *CPT1* deficiency, where affected children are at elevated risk of hospitalization and death during respiratory infectious episodes[31-33].

Results

Inhibition of CPT1 prevents secretion of diverse peritoneal oxylipins in vivo

Mitochondrial β-oxidation of native long chain FA requires uptake of their FA-CoA derivatives *via* the outer membrane transporter, carnitine palmitoyltransferase-1 (CPT1), of which there are three isoforms, a,b,c. However, whether oxylipin species can be imported via CPT1 in macrophages is unknown. To test this *in vivo*, the pan CPT1 inhibitor etomoxir was injected IP into wild type C57BL/6 mice alone or with the bacterial lipid lipopolysaccharide (LPS 1 μg), then peritoneal lavage harvested after 6 hrs, and analyzed using LC/MS/MS. A large number of oxylipins were detected in cell-free supernatant with

several showing strong elevations in response to LPS alone (Figure 1). These are broadly categorized into lipids from 12/15-LOX, COX-1/2 or CYP450, although some are from more than one pathway (Supplementary Table 1). Specialist pro-resolving mediators (SPM) such as resolvins or protectins were not conclusively detected. For maresin1 (7*R*,14*S*-diHDOHE), two peaks were seen with one having the same retention time as the authentic standard (Supplementary Figure 1 A). However, it wasn't possible to generate a convincing MS/MS spectrum from tissues, that matched standard. The presence of two isomers suggests diastereomers of 7,14-di-HDOHE, and the peaks may also contain co-eluting stereoisomers. Thus, this lipid is named 7,14-diHDOHE.

Etomoxir stimulated small increases in several oxylipins, however when included with LPS, a far stronger impact was seen, and many lipids were effectively doubled (Figure 1 A,B). This suggests that peritoneal mitochondria actively metabolize bioactive oxylipins in health, but following an acute infectious stimulus, their role is significantly enhanced (Figure 1 A,B).

CPT1 regulates metabolism of endogenously-generated oxylipins by peritoneal macrophages.

In vivo, peritoneal oxylipins could be metabolized by mitochondria in resident macrophages, B cells and/or peritoneal membrane (mesothelium). Naïve resident macrophages, which express COX-1 and 12/15-LOX (*Alox15*), are likely to be the primary basal source [34]. Thus, naïve peritoneal macrophages from wild type or *Alox15*$^{-/-}$ mice were assessed for mitochondrial removal of endogenously oxylipins. We focused on secreted forms, since most are released to activate GPCRs extracellularly. No serum was present, since this contains significant amounts of oxylipins. LPS (24 hrs) robustly stimulated prostaglandin and thromboxane secretion by naïve resident peritoneal macrophages, consistent with COX-2 induction (Figure 2 A,B,D). Although 12/15-LOX is

highly expressed in naïve peritoneal macrophages, its loss in culture leads to relatively low generation of monohydroxy FA (12-HETE and 12/15-HEPEs), with these being absent in *Alox15*$^{-/-}$ macrophages (Figure 2 C) [35]. Overall, oxylipin species generated by peritoneal macrophages were similar to those in lavage, although the total number/diversity was less with fewer CYP-derived species and no SPMs detected (Figures 1,2).

Etomoxir significantly increased macrophage secretion of several mono-hydroxy lipids and all COX-2 products (Figure 2 B-E, Supplementary Figure 1 B,C). This indicates that both their formation and removal is increased by inflammation, similar to *in vivo* (Figure 2 A,B,D). *Alox15* deletion did not impact COX-2 product levels indicating lack of substrate competition between LOX and COX (Figure 2 A,B,D). 12-HETE, 12-HEPE and 15-HEPE increased with etomoxir in WT cells but were suppressed by LPS likely due to inflammation-associated loss of 12/15-LOX during the 24 hr culture (Figure 2 C) Importantly, *in vivo* or *in vitro*, COX-2 and 12/15-LOX products were consistently increased by CPT1 inhibition.

Several mono- and di-hydroxy oxylipins were only detected when CPT1 was blocked indicating that their mitochondrial metabolism exceeds their generation (Figure 2 E, Supplementary Figure 1 C). Thus, CPT1 prevents their secretion under basal and inflammatory conditions. On the contrary, during LPS challenge, the eicosapentaenoic acid (EPA) product 17,18-diHETE, generated by soluble epoxide hydrolase oxidation of CYP-derived 17,18-EET, was suppressed by etomoxir (Supplementary Figure 1 D). Overall, these data indicate that peritoneal macrophage oxylipin generation by 12/15-LOX or COX-2 is dynamically counterbalanced by CPT1-mediated uptake into mitochondria, dampening their extracellular secretion. However, CYP-derived lipids show the opposite, requiring CPT1 for their formation. Potential reasons could include that β-oxidation generates essential substrates for FA synthase (FAS)/elongase activities required for oxylipin polyunsaturated FA (PUFA) substrate generation (see discussion).

Bone marrow derived macrophages consume diverse oxylipins from serum.

Macrophages are exposed to oxylipins from other immune or stromal cells during inflammation. Serum contains numerous oxylipins from 12-LOX and COX-1, primarily mono-hydroxy isoforms and thromboxane, generated by white cells and platelets, but few prostaglandins (PGs). It is a physiological biofluid formed during innate immunity thus metabolism of serum oxylipins could impact their signaling at local or systemic sites. To examine this, we tested primary murine bone marrow-derived cells differentiated to macrophages, then then treated with M-CSF, LPS/IFNγ or IL-4 (henceforth referred to as M0, M1 and M2) respectively as *in vitro* of models for macrophage inflammation [36]. All macrophage phenotypes consumed significant amounts of exogenous mono-hydroxy oxylipins from 10 % serum-containing medium, including 12-HETE/12-HEPE (12-LOX, generated by platelets), 5-HETE/5-HEPE (5-LOX, generated by neutrophils) and 9-/13-HODEs (Figure 3 A-C). 11-HETE/11-HEPE and 15-HETE/15-HEPE were removed by M0(M-CSF) and M2(IL-4) cells, however they appeared higher or unchanged for M1(LPS/IFNγ), since they were simultaneously generated by COX-2, induced by LPS/IFNγ (Figure 3 A,B). Furthermore, M1(LPS/IFNγ) cells secreted large amounts of PGs and thromboxane due to COX-2, causing a net increase in their extracellular levels. (Figure 3 D-E). Thus, the overall pattern was consumption of serum oxylipins by all macrophage populations, coupled with simultaneous generation of COX-2 PGs by M1(LPS/IFNγ). Last, low dose etomoxir (25 μM) significantly increased PGs released by M1(LPS/IFNγ) cells (Figure 3 F). Overall, this demonstrates that mitochondrial uptake of PGs suppresses their secretion from classic inflammatory BMDM cells (M1(LPS/IFNγ)), in the same manner as seen with naïve peritoneal macrophages and *in vivo* with LPS peritonitis, while all BMDM cell types consume significant amounts of HETEs and HEPEs.

Dynamic control of oxylipins by CPT1 during inflammatory challenge in RAW macrophages.

Next, we switched to RAW cells, a model for macrophage inflammatory responses *in vitro*, highly amenable to genetic modification. RAW cells do not express 12/15-LOX, therefore cells stably overexpressing *Alox15* (RAW*Alox15*) were generated. Basally, neither RAW or RAW*Alox15* cells secreted many oxylipins, with only 9/13-HODE, two PGs, and two di-hydroxy products of CYP released in low amounts (Figure 4 A). LPS (24 hrs, 100 ng/ml) stimulated robust secretion of many oxylipins including several PGs (COX-2) 9/13-HODEs, and 11- and 15-HETEs, HETrEs and HEPEs (likely COX-2) (Figure 4 A). The primary 12/15-LOX products 12-HETE and 14-HDOHE were only detected in RAW*Alox15* cells, and their generation was increased by LPS (Figure 4 A.B).

CPT1 inhibition had little impact on basal oxylipin secretion (Figure 4 A). However, it significantly elevated LPS-dependent generation of mono-hydroxy FA (HETEs, HDOHEs, HETrEs and HODEs) from RAW*Alox15* cells (Figure 4 B-F). These data indicate that secreted oxylipins normally represent only a fraction of the overall amounts made by 12/15-LOX, with large amounts dynamically removed by mitochondria. Thus, LPS increases CPT1-mediated removal of 12/15-LOX products, similar to *in vivo* and peritoneal macrophages (Figures 1,2). Here, many are primary 12/15-LOX products (12-HETE, 14-HDOHE), while others (9-HOTrE, 9-HETE, 9-HODE), may be biproducts of secondary propagation reactions. In etomoxir/LPS-treated RAW cells, a lipid suggestive of resolvinD5 (7S,17S-diHDOHE) was seen, however of the two peaks detected, only one matched the retention time of the authentic standard (Supplementary Figure 1 E). The lipid was very low abundance, and it was not possible to generate a reliable MS/MS spectrum from cell supernatants. As there were two peaks, they may represent diastereomers of 7,17-di-HDOHE, and the individual peaks may also contain co-eluting stereoisomers. Thus, we labelled this 7,17-diHDOHE (Supplementary Figure 1 E) and suggest it arises from non-enzymatic oxidation. No SPMs were detected in any other samples from RAW or RAW*Alox15* cells.

Several COX-2 derived PGs and 17,18-diHETE (CYP) were significantly decreased by etomoxir (Figure 4 G,H, Supplementary Figure 1 F). This mirrored the impact of CPT1 inhibition on peritoneal macrophage 17,18-diHETE (Supplementary Figure 1 D). Overall, LOX products were consistently elevated by etomoxir in RAW cells or all primary macrophages tested, however for RAW cells both COX and CYP-derived lipids were instead suppressed.

Exogenous 12-HETE is metabolized to diene and triene tetranor metabolites via mitochondrial and non-mitochondrial β-oxidation in RAW cells

To determine the fate of oxylipins removed by CPT1, we examined metabolism of exogenous 12-HETE by RAW macrophages. 12(S)-HETE was rapidly removed following LPS-stimulation, coinciding with formation and subsequent metabolism of two tetranor 12-HETEs (Figure 5 A-C). These were confirmed by MS/MS as a triene, 8-hydroxy-4Z,6E,10Z-hexadecatrienoic acid (comparison with authentic standard), and a diene, proposed as 8-hydroxy-6,10-hexadecadienoic acid (through comparison with [37]) (Supplementary Figure 2 A-C). Both will be 8(S) since they originate from 12(S)-HETE. As confirmation, 12(S)-HETE-d8 was added to RAW cells (3 hrs), and a deuterated diene was detected (Supplementary Figure 2 D,E). The MS/MS fragmentation of these lipids is shown (Schemes 1-3). For the tetranor diene, fragmentation matched expected gas phase chemistry of hydroxylated FAs, where cleavage occurs next to the hydroxyl group (Schemes 2,3). For the triene, a daughter ion at *m/z* 165.1 was seen, with high resolution MS/MS of the standard confirming this as $C_{11}H_{17}O$ (Supplementary Figure 3 A,B, Scheme 1). NMR for the triene is shown in Supplementary Figure 4. Almost all triene and diene was detected extracellularly, and over 4-8 hrs, both disappeared from supernatant and cell pellets (Figure 5 B,C). This reveals that macrophages generate and secrete primary and secondary metabolites of HETEs, but then re-internalize them for further metabolism. We next

incubated triene tetranor 12(S)-HETE with RAW macrophages, and after 3 hrs, the diene was detected extracellularly (Supplementary Figure 3 B). This indicates that diene forms via saturation of the triene, confirming the structure as 8(S)-hydroxy-6E,10Z-hexadecadienoic acid.

Next the impact of CPT1 inhibition on metabolism of exogenous 12-HETE was tested. Both 12(S) and 12(R) isomers were used to determine the impact of chirality. For 12(R)-HETE, the tetranors will be 8(R)-hydroxy. 12-HETE was rapidly removed by LPS-stimulated RAW cells, with around 0.15% or 0.4% remaining after 3 hrs for S or R enantiomers respectively (Figure 5 D,E). Cellular and supernatant 12(S)- and (R)-HETEs were increased by CPT1 inhibition, although the primary removal appeared to be non-mitochondrial since only a small amount was recovered (Figure 5 D,E). As before, most 12-HETE was extracellular, although intracellular and supernatant levels were both increased by etomoxir. 12-HETE was efficiently converted to tetranor trienes and dienes, which were detected mainly outside (Figure 5 F-I). These were around 5-8-fold increased by CPT1 blockade, confirming that they are also dynamically metabolized by mitochondria in LPS-stimulated macrophages.

CPT1a gene silencing confirms dysregulation of oxylipin secretion in RAW cells.

Considerably higher amounts of etomoxir than used here (~10-fold higher) can have off-target effects due to an impact on adenine nucleotide translocase and CoA [38, 39]. To rule this out, we targeted CPT1a using a lentiviral approach. Silencing to around 14 % control levels was achieved in RAW264.7 macrophages, stably expressing shRNA that targets *Cpt1a (*RAW*Cpt1a*^{KD}), but not those expressing a non-silencing control (RAW^{nonsil}) (Supplementary Figure 5 A). CPT1 maintains mitochondrial health since it imports FAs to maintain cardiolipin and phospholipid pools inside mitochondria[40]. Thus, CPT1-deficient cells do not proliferate normally and may alter their bioenergetic and lipid metabolism

profiles. The balance between mitochondrial and peroxisomal β-oxidation and their ability to support FAS/elongase activities required to generate PUFA for oxylipin synthesis may have adapted. Similar to low dose etomoxir, the overall impact on endogenous LPS-stimulated PG synthesis in RAW cells was suppression of supernatant and cell levels (Figure 6 A,B). Furthermore, the most abundant CYP450 product (17,18-diHETE) was suppressed, as also seen for etomoxir with naïve peritoneal macrophages and RAW cells (Figure 6 C). Endogenous generation of several monohydroxy eicosanoids was suppressed by silencing of *Cpt1a* (Figure 6 D). This data further confirms the dual role of CPT1 in both generation and removal of oxylipins depending on their enzymatic source and cell type.

RAW cells do not generate 12-HETE, thus its metabolism when exogenously added was tested. This also allowed mitochondrial oxylipin removal to be determined in isolation. In basal RAW cells, *Cpt1* knockdown did not prevent metabolism of 12-HETE, instead there was a non-significant increase, presumably by compensatory peroxisomal or other pathways (Figure 6 E). In contrast, 12-HETE removal by LPS-stimulated RAW cells was significantly inhibited by *Cpt1* knockdown (Figure 6 E). Furthermore, the triene and diene tetranor metabolites were significantly reduced by *Cpt1* knockdown in LPS-treated but not basal RAW cells (Figure 6 F,G). This indicated that following *Cpt1* knockdown, RAW cells showed reduced mitochondrial metabolism of 12-HETE coupled with lower formation of its tetranor products following LPS stimulation.

Inflammation accelerates 12-HETE conversion to triene tetranor 12-HETE via mitochondrial β–oxidation in vivo.

Earlier, *in vivo* inhibition of CPT1 was seen to significantly elevate many oxylipins in the peritoneal cavity following LPS challenge. To examine β-oxidation of oxylipins via mitochondria *in vivo*, the formation of tetranor metabolites was next measured. The diene metabolite was absent, however tetranor 12-HETE triene was significantly elevated on

CPT1 blockade, but only during inflammatory stimulation (Figure 7 A). This confirms that inflammation *in vivo* not only increases formation and mitochondrial uptake of oxylipins (shown in Figure 1), but also their metabolism to tetranors (Figure 7 A).

Oxylipin metabolism by mitochondria is not sustaining oxidative phosphorylation (OxPhos).

Mitochondrial β-oxidation of FA is linked with OxPhos through several checkpoints. It forms acetyl-CoA, a substrate for the TCA cycle as well as NADH and $FADH_2$, substrates for complexes I and II, and also electrons transfer to flavoprotein-ubiquinone oxidoreductase (ETF-QO)[41]. Thus, oxylipins could contribute to OxPhos. However, LPS suppresses mitochondrial respiration, through multiple mechanisms including aconitase inhibition and nitric oxide binding to complex IV making this unlikely[28]. Indeed, here LPS treatment profoundly decreased cellular respiration consistent with previous data (Figure 7 B,C) [42, 43]. Importantly, LPS did not impact mitochondrial DNA (mtDNA), or cause organelle damage as measured by DNA lesion frequency (Figure 7 D,E). Thus, mitochondria are still present in LPS-treated cells, although β-oxidation of FAs is largely uncoupled from OxPhos.

Oxylipin elevation following CPT1 inhibition enhances neutrophil phagocytosis.

In vivo inhibition of CPT1 doubled many oxylipins detected in inflammatory peritonitis, thus mitochondrial β-oxidation might impact their signaling (Figure 1). To address this, human phagocyte responses to oxylipins were determined. Here, ROS production elicited by *S. epidermidis*, a common pathogen in human peritonitis was measured by APF fluorescence of whole blood leukocytes [44]. Two concentrations were used that represented amounts of 52 individual oxylipins detected *in vivo,* in the presence or absence of etomoxir (with LPS) (Figure 1, Supplementary Table 2). Here, ROS generation by neutrophils was consistently enhanced by higher or lower oxylipin levels. However, there was a significant concentration-dependent impact in three individual donors (Figure 7 E,G). Thus, the higher amount,

consistent with levels detected during CPT1 inhibition, was significantly more potent at activating neutrophils. Monocyte ROS generation was unaffected at either dose (Figure 7 F,H). These data support the concept that oxylipin removal by mitochondria during inflammation can regulate cellular innate immune responses.

Transcriptional analysis of human neonatal bacterial sepsis identifies gene candidates responsible for mitochondrial oxylipin metabolism

The enzymes that import oxylipins into mitochondria are currently unknown, but it is very likely that those importing long chain FA are involved. These include five acyl-CoA synthetase long-chain family members (*ACSL1,3-6*), as well as *CPT1a, 1b, 1c*, and *CPT2.* These mediate formation of -CoA and then -carnitine derivatives that are required for long chain FA uptake across mitochondrial membranes (Figure 8, Supplementary Table 3). Next, enzymes form the mitochondrial β-oxidation pathway for long chain FA mediating sequential removal of 2C fragments to generate acetyl-CoA, and chain shortened metabolites. These include *HADHA, HADHB, ECI1, DECR1 and ACADVL* (Figure 8, Scheme 4, Supplementary Table 3) [22]. A set of 32 genes were compiled including also those isoforms with preference for medium or shorter chain FA. Their expression during human infection *in vivo* was tested using a microarray from human neonatal whole blood cells (35 cases, 26 controls). Here, infants suspected of infection had blood cultures conducted, and a diagnosis of bacterial sepsis obtained[45]. Out of the genes tested, 22 were significantly different with 9 up- and 13 down-regulated in sepsis (Supplementary Table 3). Notably, several upregulated genes were involved in generation of long chain FA-CoAs and their interconversion to acyl-carnitines in mitochondria. For the most relevant, 7 were significantly upregulated (*ACSL1,3,4, CPT1b, CPT2, ACADVL, HADHB*) while 3 were downregulated (*ACSL5, ECI1, HADHA*) (Figure 9 A,B). This indicates a high degree of regulation during complex bacterial infection in seriously ill humans, suggesting the specific

isoforms that maybe involved in oxylipin removal. We also tested the gene set in murine bacterial peritonitis, induced using cell-free supernatant from a clinical isolate of *Staphylococcus epidermidis* (SES) [46]. Here, there was overall upregulation, showing a similar trend to the human bacterial dataset (Figure 9 C,D). Although most individual genes were not statistically significant, *Cpt1a* showed around 2-fold induction significant 6 hrs post infection (Figure 9 C,D).

A consistent upregulation of ACSL1 is revealed across multiple human and murine macrophage datasets.

Next, data from 3 mouse BMDM or 3 human PBMCs studies were downloaded from GEO [47-52]. For BMDM, *Acsl1* was consistently significantly induced on stimulation using either LPS/IFNγ or IFNγ alone (Figure 10 A,C). Two of the mouse BMDM datasets also indicated significant increases in *Eci1*, encoding 3,2-enoyl-CoA isomerase (Scheme 4, Figure 10 B). In human studies, *ACSL1* was also induced by LPS/IFNγ or IFNγ (Figure 10 D).

Discussion:

Oxylipins are soluble mediators generated during inflammation and infection that link lipid metabolism with immunity. Dynamically controlling their removal is essential to dampen inappropriate inflammation. Here we show that blocking the mitochondrial enzyme carnitine palmitoyltransferase1 (CPT1), effectively doubles secreted levels of endogenously-generated oxylipins *in vivo* during inflammatory challenge. Using exogenous 12-HETE, we establish a paradigm in which macrophage removal of oxylipins and their metabolites involves repeated cycles of secretion and re-internalization of partially-oxidized tetranor intermediates, followed by further mitochondrial metabolism (Figure 8). Extending previous studies, we found high levels of secreted free acid tetranors *in vitro* and *in vivo*, thus regardless of whether formed in peroxisomes or mitochondria, these lipids appear to

undergo repeated cycles of acylation/de-acylation (to CoA and carnitine forms, via ACSLs and CPT) facilitating their rapid secretion, re-internalization and further β-oxidation[37, 53]. This demonstrates a complex cellular metabolism for tetranors, and raises questions as to why they are secreted, instead of being simply metabolized to terminal end products.

Our finding that oxylipin metabolism is strongly stimulated by LPS has implications for the rare genetic disorder, *CPT1 deficiency*, where symptomatic episodes and death are triggered by acute infection[31]. Also, rates of hospitalization and deaths in infants with the *CPT1a* variant p.P479L are higher for homozygotes with respiratory, dental and aural infections[32, 33]. This variant reduces CPT1a activity around 50% [32, 33]. The observation that infection causes severe symptoms indicates that mitochondrial β-oxidation is a protective response to pathogen challenge. This is fully in line with our findings that CPT1-dependent oxylipin removal is elevated by the bacterial product LPS, and suggests that this maybe an important part of the physiological response to infection, functioning as an “off-switch” for pathologic signaling. Whether oxylipin levels are elevated in patients with CPT1a deficiency is not known, and future studies to examine this are warranted.

Mitochondrial uptake of short/medium chain native FAs is independent of carrier proteins, however long chain native FA require first activation to acyl-CoA derivatives by acyl-CoA synthetases (ACSL), then conversion to acyl-carnitines, via CPT1 (Figure 8). Following import into mitochondria via an inner membrane transporter, FA are re-converted to acyl-CoAs by CPT2. These are used for mitochondrial β-oxidation, with sequential removal of two C fragments, and generation of acetyl-CoA. Using a human sepsis cohort and multiple human and murine *in vitro* models, we propose a biochemical pathway for oxylipin uptake and mitochondrial metabolism during infection (Scheme 4). A consistent pattern across all studies was upregulation of *ACSL1/Acsl1*. This isoform is well known to shuttle FAs to mitochondria for β-oxidation and lipid synthetic pathways [54-60]. As yet, the specific ACSLs that acylate oxylipins are not known, although Klett found that all 6 isoforms

are active *in vitro* [61]. ACSL1 is known to be critical for shuttling FA into mitochondria for β–oxidation in heart, skeletal muscle and adipose tissues [54-58]. Furthermore, in liver, ACSL1 and CPT1 were shown to be physically associated [59, 60]. Thus, ACSL/CPT1 may be a critical checkpoint enabling higher rates of oxylipin metabolism during infection. Indeed, a critical role for ACSL1 in sepsis outcome has been proposed [62]. Two other long chain metabolizing *ACSLs* (3,4) were induced in human sepsis, indicating multiple complex mechanisms of isoform regulation. Regulating import of long chain FAs into the mitochondrial matrix, we found increased *CPT1a or b*, dependent on the model, along with *CPT2* induction in human sepsis. Murine BMDM stimulated with IFNγ also upregulated *Eci1*. This encodes DCI, which converts 3-cis or trans-enoyl-CoA to 2-trans-enoyl-CoA during mitochondrial β-oxidation and was previously shown to be induced during HCV infection and required for virus replication [63, 64]. Last, upregulation of the β-subunit of the mitochondrial trifunctional protein (*HADHB*) and very long chain acyl-CoA dehydrogenase (*ACADVL*) are also fully consistent with their proposed role in oxylipin β-oxidation (Scheme 4).

Macrophages rely primarily on glycolysis for energy when stimulated with LPS/IFNγ, and conversely use FAO to supply OxPhos with substrates, when exposed to "anti-inflammatory" stimuli such as IL-4[26]. However, recent studies have uncovered a significant role for lipid metabolism in "M1" cells even in the absence of OxPhos, with FA synthetic pathways (FAS) being upregulated by LPS[26]. This anabolic event is proposed to supply inflammatory activated cells with lipids for processes such as proliferation (sphingolipids, glycerolipids, phospholipids, etc), and generation of oxylipins[26]. Here, we focused down on inflammatory activated macrophages that generate oxylipins, where metabolism will favor glycolysis and FAS, and reduced OxPhos. We show for the first time that CPT1 mediates exogenous and endogenously-generated oxylipin β-oxidation by

macrophages, that is elevated during inflammation. The impact of blocking CPT1 varied by sub-family of oxylipins, based on either:

(i) Cell type. Etomoxir consistently elevated LOX-derived oxylipins and various other mono-hydroxy-oxylipins, while suppressing CYP/sEH metabolites in all macrophages (Figures 2-4). However, COX-derived PGs increased *in vivo* and in primary macrophages, but were suppressed in RAW cells (Figures 1-4).

(ii) *How CPT1 was targeted.* In RAW cells, etomoxir or gene silencing suppressed COX-derived PGs and CYP/sEH oxylipins. In contrast, monohydroxy oxylipins were increased by etomoxir but suppressed by CPT1 knockdown in RAW cells (Figure 4). Etomoxir was used at 25 μM, well below that found to induce off target effects on adenine nucleotide translocase [38, 39]. Indeed, previous studies using high levels led to FAO being incorrectly proposed as required for alternative activation of M2 macrophages (100-200 μM)[65]. Nowadays, lower concentrations are recommended that block ~90% of β-oxidation without side-effects (e.g. 10 - 25 μM)[40]. As a second approach, shRNA knockdown stably reduced expression of CPT1a. However, this causes adaptive changes to the metabolic status of macrophage mitochondria, beyond acute inhibition of CPT1. Recent publications implicate CPT1 in maintaining mitochondrial health due to its requirement for importing FAs for maintaining mitochondrial cardiolipin and phospholipid pools [40]. Thus, cells lacking CPT1 do not proliferate normally and may have adapted to a deficiency in OxPhos through alterations in other lipid and energy metabolism pathways. Thus, constitutive knockdown may directly impact the balance between mitochondrial and peroxisomal β-oxidation and the ability to support FAS/elongase activities in the cells. Nevertheless, both inhibitory approaches caused significant changes to oxylipin secretion, both for PGs, 12-HETE and its two tetranor metabolites, supporting the hypothesis that mitochondria can be a significant site of oxylipin regulation in macrophages.

Our data reveal complex modulation of oxylipin removal and formation by CPT1 as follows:

(i) Removal: Oxylipins and their metabolites can be degraded by two separate β-oxidation pathways, with only mitochondrial enzymes relying on CPT1. However, peroxisomes and mitochondria display metabolic interplay where FA degradation intermediates are transferred for metabolism between the organelles[66]. Thus, stable knockdown of CPT1 may require compensatory increases in peroxisomal β-oxidation. It has been proposed that truncated unsaturated FA metabolites may need to transfer to mitochondria for complete metabolism[66]. Indeed, 12-HETE-triene was suggested as the terminal peroxisomal metabolite for 12-HETE, with further metabolism proposed to require mitochondria[18]. Our data provide direct evidence for this interplay between organelles, since blockade of CPT1 had a far greater impact on metabolism of tetranor metabolites than exogenous 12-HETE in LPS stimulated cells (Figure 5). Thus, 12-HETE can be metabolized in either organelle, but peroxisomal-generated tetranors are then shuttled to mitochondria, with their oxidation significantly stimulated by inflammation.

(ii) *Generation*: FA synthesis was proposed to be required for oxylipin generation in LPS-stimulated cells[67]. This is because FAS and FA elongases require TCA intermediates (malate, citrate, acetate), which themselves depend at least in part on CPT1 for formation. Thus, while both synthesis and degradation of oxylipins simultaneously occur in macrophages, steady state levels will depend on the cells' metabolic status, and whether CPT1 is mainly supporting degradation (by β-oxidation) or synthesis (by supplying TCA intermediates) of individual oxylipins. Thus, CPT1 could either increase or decrease levels of oxylipins and their metabolites concurrently, as seen in our study. A detailed flux analysis of this phenomenon is required to further our understanding.

Here, we show that mitochondrial oxylipin removal takes place during inflammation on a background of reduced OxPhos, a well-known response to LPS stimulation by macrophages [28]. However, β-oxidation requires a basal level of OxPhos both to

regenerate NAD+ and oxidized flavin cofactors in the electron transferring flavoprotein complex, that reduces ubiquinone directly. While OxPhos was suppressed, there was a low residual activity remaining in both RAW and peritoneal cells that appeared sufficient to sustain β-oxidation, observed by formation/metabolism of oxylipins and HETE tetranors. Our experiments using exogenous 12-HETE suggest that non-mitochondrial oxidation is probably responsible for removing most. This agrees with previous studies where exogenous 12-HETE added to mammalian cells was removed by peroxisomes forming a series of metabolites, down to C12:1 [18, 37, 68, 69]. However, these studies did not consider the impact of inflammation and the focused was exclusively on exogenous 12-HETE, not endogenous oxylipins generated by the cells. Here, we extend this to the whole range of oxylipins generated by macrophages, and reveal that during LPS-inflammation, mitochondria (via CPT1) effectively halve secreted amounts of oxylipins en masse, and are a key site for removing peroxisomal metabolites of 12-HETE. We demonstrate that this alters the outcome of leukocyte activation, suggesting that mitochondrial β-oxidation may act as a brake for dampening host inflammatory responses *in vivo* during infection. The potential implications for humans with CPT1a deficiency, relating to severely augmented inflammation during infection should be considered and studies initiated to test this idea. Also, whether this phenomenon contributes to infection-associated host inflammation in general, in cases where mitochondrial health is compromised, should be considered.

Methods

Mouse peritonitis model

All mouse experiments were performed in accordance with the United Kingdom Home Office Animals (Scientific Procedures) Act of 1986 (P05K6A456). Wild-type (WT) female C57BL/6 mice were purchased from Charles River Laboratories. Mouse breeders were housed in isolators and experimental mice in individually ventilated cages with 12-h light/dark cycles and controlled temperature (20 – 22 °C). Access to water and standard chow was ad libitum. *Alox15* deficient mice were as previously described, but backcrossed to F11[70]. Female C57BL/6 mice wild type or *Alox15*$^{-/-}$ mice (7-9 weeks) were injected intraperitoneally with etomoxir (100 µg, Sigma Aldrich) and/or LPS (1 µg, E.Coli 0111.B4, Sigma-Aldrich) or vehicle (PBS) per mouse. After 6 hr, mice were peritoneally lavaged using 5 ml ice cold PBS (with 5 mM EDTA). Eicosanoid internal standard mix was added to the lavage solution (7.5 ml per 5 ml lavage solution, Supplementary Table 4). Cells were removed by centrifugation and resuspended in 1 ml PBS. Supernatant and cells were frozen at -80 °C until lipid extraction using solid phase as described below.

Isolation and treatment of resident peritoneal macrophages

Wild type and *Alox15*$^{-/-}$ mice (female, 9-13 weeks) were lavaged with PBS supplemented with 5 mM EDTA, and peritoneal cells from 4 - 5 mice pooled together. A small amount was labelled with F4/80 (BD Horizon, BV421 Rat Anti-Mouse F4/80, Clone T45-2342, Cat.: 565411) and CD11b-allophycocyanin antibodies (BD Pharmingen, Clone M1/70, PE Rat Anti-Mouse, Cat 557397), both 0.2 µg/ml final concentration, to determine macrophage numbers. Cells were first blocked for non-specific antigen binding (incubating for 20 min at RT with 2 µg/ml CD16/CD32 Rat anti-Mouse, unlabeled, Clone: 2.4G2, BD) then antibodies were added without washing off the blocking solution, and cells were incubated for further

20 min at RT. Cells were then centrifuged for 5 min at 1500 rpm, 4C, supernatant discarded and cells resuspended in 150 µl PBS and % macrophages determined using flow cytometry. Peritoneal cells were seeded at 10^6 macrophages/well of a 6-well plate and cultured in DMEM (with 10 % heat inactivated FCS and pen/strep), for 2 hours at 37 °C, 5 % CO_2, 99 % humidity. Nonadherent cells were removed by washing with media, and the remaining cells cultured in serum free RPMI, with/without LPS (100 ng/ml) and/or etomoxir (25 µM). After 24 h, cells and supernatants were harvested separately, with supernatant first centrifuged (1500 rpm, 5 min, 4 °C), and cells scraped quickly into 1 ml RPMI and stored at -80 °C, prior to lipid extraction and analysis.

Generation and culture of RAW264.7 cell lines stably overexpressing Alox15, or expressing shRNA targeting Cpt1a.

Alox15 overexpressing RAW264.7 cells were generated by retroviral transduction using the pMX-IP retroviral vector, which is based on the Moloney Murine Leukemia Virus (MMLV) [71]. Briefly, mRNA was extracted from C57BL/6 peritoneal cells, and *Alox15* was PCR amplified with the following primer sequences:

- Alox15-Fw TCCTGCAGGCCTCGAGCCACCATGGGTGTCTACCGCATCC
- Alox15-Rv: CGCGCCGGCCCTCGAGTCATATGGCCACGCTGTTTT

The In-fusion cloning kit (Takara Bio) was utilized to insert *Alox15* into the *Xho I* site of the pMXs MMLV retroviral plasmid. Retroviral particles were generated after transfection of HEK293T cells with the viral plasmid. RAW264.7 cells were spin-infected with packaged retrovirus (*Alox15* or empty vector control pMXs-IP). Positive infections were selected by resistance to 3 µM puromycin, screened for positive *Alox15* expression by PCR (Supplementary Figure 5 B). Separately, RAW264.7 cells were infected with lentiviral vectors to generate *Cpt1a* knockdown or non-silencing control cell lines, as described [72]. Alterations from the published method were different lentiviral plasmids (pSMART

mEF1a/TurboGFP (Cpt1a targeting shRNA [V3SVMM03-13316872] and non-targeting control) - Dharmacon). Briefly, lentiviral particles were created by transfecting HEK293T cells (lentiviral plasmid plus helper constructs (pCMV-Δ8.91 (Gag/Pol, Tat and Rev) and pMD2.G (VSV-G coat)) using the Effectene transfection reagent (Qiagen). Lentivirus was concentrated 48 h after transfection from 0.45 µm filtered supernatants layered on top of 1/6th volume of 0.584 M sucrose using a Beckman Coulter Ultracentrifuge (100,000 x g, 90 min, 4 °C). Lentiviral particles concentrated from 20 ml of supernatant were added to a ~10 % confluent RAW264.7 cells in a T-175 flask for 3 days. After another 4 days of subsequent cell expansion positively infected cells were sorted using GFP expression on a BD FACS Aria cell sorter (100 µm nozzle size) (Supplementary Figure 5 C,D. Knockdown was validated by real-time PCR. Mature *Cpt1a* mRNA target sequence: CAGTGGTATTTGAAGCTAA, the sequence of the non-targeting control was not disclosed by Dharmacon but is validated to have minimal targeting to known mouse genes. To confirm knockdown, RNA was extracted using the PureLink RNA extraction kit, cDNA was created using the high capacity reverse transcription kit (Life Technologies). Real-time PCR was performed using the Taqman assay (Applied Biosystems) on a Stratagene MX3000P real-time PCR instrument. Data was analyzed using the ΔΔCt method, normalizing *Cpt1a* (probe spans exons 13-14: Mm01231183_m1) gene expression to the housekeeping gene *Hprt* (probe spans exons 2-3: Mm03024075_m1) (Supplementary Figure 5 A). RAW cells were cultured in DMEM with 10 % FCS and pen/strep. Cells were passaged at ~80 % confluency using PBS with 5 mM EDTA and 27.7 mM lidocaine for ~5 min at 37 ^{0}C. Cells were cultured with/without 100 ng/ml LPS, with/without 25 µM etomoxir for 24 h in serum free RPMI medium. Then cells and supernatants were harvested separately and stored at -80^{0}C until lipid extraction and analysis using LC/MS/MS.

Bone marrow derived macrophages (BMDM) isolation and differentiation. Bone marrow cells were harvested from femurs and tibias of mice (8-10 weeks old, female C57BL/6) using syringe flushing. After centrifugation and washing twice with PBS cells were plated at 2 x 10^5/ml in DMEM (10% FCS, +/- 5 % horse serum, pen/strep, L-glutamine, +/- Hepes). MCSF was added at final concentration 20 ng/ml. On day 3, cells were refed using media and MCSF. On day 7-8, cells were washed with PBS, then lifted with lidocaine/EDTA or ACCUTASE™ (Sigma-Aldrich), plated at 1 - 2 x 10^6 per well of a 6-well plate and rested for 24 h. Cells were washed and then refed with DMEM (as above, with MCSF) and cytokines as follows: M0: medium only, M1: LPS (100 ng/ml)/IFNγ (20 ng/ml), M2: IL-4 (20 ng/ml). For some experiments, FCS was omitted. Etomoxir (25 μM) was added in some experiments. After 24 hrs supernatant was recovered and frozen at -80 ºC. Cells were washed and then recovered in 1 mL of PBS using rapid scraping on ice, and the cell suspension immediately quenched in liquid N_2 prior to storage at -80 °C.

Samples were analyzed for phenotype confirmation (cytokine production, mRNA gene expression by real time PCR) and lipid composition, as described. CCL5, TNFα and IL-6 in supernatants were measured using ELISAs (Mouse TNFα; Mouse CCL5; Mouse IL-6, R&D Systems) according to the manufacturer's protocols. Confirmation of phenotype is shown in Supplementary Figure 6 A,B. Total RNA was recovered using the RNeasy Mini Kit (QIAGEN) according to the manufacturer's instructions. RNA concentration and purity were determined using a Nanodrop spectrophotometer. cDNA was prepared from 1 μg of RNA. RNA was reverse-transcribed using superscript III reverse transcriptase (Invitrogen) in a total volume of 20 μL for 1 h at 50 °C, and the reaction was terminated at 70 °C for 15 min. Power SYBR® Green PCR Master Mix (Thermo Fisher scientific) was used for real-time PCR. The Master Mix (10 μL) was added to dH2O (7.5 μL), and 1 μl primer mix (0.5 μg/mL each primer) to make a gene specific master mix; cDNA (1.5 μL) from each sample was

added to the reaction mix (17.5 µL) in a 96-well plate well. The plate was inserted into a QuantStudio 3 Real-Time PCR system and the PCR amplification started as per instrument instruction: 50°C – 2 min; 95°C - 10 min; 95°C - 15 s; 60 °C - 1 min; Repeat 3 - 4 for 40 cycles; 95 °C - 15 s; 4 °C end. Primers used for real-time PCR were designed to be intron-spanning, and to have a melting temperature 55 - 65 °C. The intron-spanning aspect ensured that only mRNA and not genomic DNA were amplified. All primers and oligonucleotides were obtained (Sigma, Gillingham UK) as salt free purified lyophilized DNA. The sequences of the real time PCR primers used were:

Gene	Forward Primer	Reverse Primer
TNF-α	AATGGCCTCCCTCTCATCAG	GTGGTTTGCTACGACGTGG
CD11c	ACGCTTACCTGGGTTACTCC	AAGATGACAACCTTCCCCGT
Arg1	ACAAGACAGGGCTCCTTTCA	TGCCGTGTTCACAGTACTCT
B-actin	TGGCACCACACCTTCTACAA	AGGTCTCAAACATGATCTGGGT

*Metabolism of exogenous 12-HETE and 12-HETE-d8 by RAW cells***.** RAW cells (2 x 10^6/ml media) were supplemented with 9 µM 12(S)-HETE, 12(S)-HETE-d8, 12(R)-HETE tetranor 12(S)-HETE (from Cayman Chemical) for up to 12 hrs in serum free RPMI, with 100 ng/ml LPS, with/without 25 µM etomoxir. Amounts supplemented were (per 10^6 cells): 12h LPS: 12(S)-HETE: 1.44 µg, 3 h LPS + Etomoxir: 12(S)-HETE/12(R)-HETE: 1.515 µg, 12(S)-HETE d8: 1.47 µg, Tetranor 12(S)-HETE triene: 1.198 µg. Cells and supernatants were harvested separately, and stored at -80 °C. Lipids were extracted as described above, using solid phase C18 columns, resuspended in small volumes of methanol and stored at -80 °C until analysis using LC/MS/MS.

Lipid extraction: Internal standard mixture (see eicosanoid assay for details, Supplementary Table 4) was added to each sample before extraction. Oxylipins were extracted from cells by adding 2.5 ml of solvent mixture (1M acetic acid/2-isopropanol/hexane (2:20:30, v/v/v) to 1 ml of sample, followed by vortexing for 60 s, and then adding 2.5 ml of hexane. The mixture was vortexed again for 60 s, centrifuged at 500 g, 4 °C for 5 min, and lipids recovered in the upper organic solvent layer. The lipids were reextracted by adding another 2.5 ml of hexane, followed again by vortexing and centrifugation. The lipids were again recovered in the upper organic solvent layer. The combined hexane layers were dried by vacuum and resuspended in methanol. Oxylipins were extracted from supernatants using solid phase extraction (SPE) using C18 columns (Sep-Pak C18, Waters). Columns were activated using 12 ml methanol, followed by 6 ml acidified water (0.4 % glacial acetic acid in HPLC water) followed by loading the sample (all samples were in 85 % aqueous, 15 % methanol, pH 3.0), and washing with 6 ml of hexane. The columns were left to dry for 15 - 20 min followed by eluting the lipids with 8 ml methyl formate. The lipids were vacuum dried, resuspended in methanol and stored at -80 °C. Lipids from supernatants were extracted by solid phase extraction, following the procedure outlined above.

LC-MS/MS targeted analysis of oxylipins

Targeted lipidomics analysis of 93 oxylipins was performed on a Nexera liquid chromatography system (Nexera X2, Shimadzu) coupled to a 6500 QTrap mass spectrometer (AB Sciex) as described, with minor adaptations[73]. Briefly, liquid chromatography was performed at 45 °C using a Zorbax Eclipse Plus C18 (Agilent Technologies) reversed phase column (150 × 2.1 mm, 1.8 µm) at a flow rate of 0.5 mL/min over 22.5 min. Mobile phase A was (95 % HPLC water/5 % mobile phase B; v/v and 0.1 % acetic acid) and mobile phase B was acetonitrile/methanol (800 ml + 150 ml; and 0.1 % acetic acid). The following linear gradient for mobile phase B was applied: 30 % for 1 min,

30 - 35 % from 1 to 4 min, 35 – 67.5 % from 4 to 12.5 min, 67.5 – 100 % from 12.5 to 17.5 min and held at 100 % for 3.5 min, followed by 1.5 min at initial condition for column re-equilibration. Injection volume was 5 µL. Lipids were analyzed in scheduled multiple reaction monitoring (MRM) mode with a detection window of 55 s for each analyte. Ionization was performed using electrospray ionization in the negative ion mode with the following MS parameters: temperature 475 °C, N_2 gas, GS1 60 psi, GS2 60 psi, curtain gas 35 psi, ESI voltage -4.5 kV. Cycle time was 0.4 s. Peak areas for lipids were integrated and normalized for deuterated internal standards and quantification was performed using external calibration curves with authentic standards for all investigated oxylipins. Data integration and quantification was performed using MultiQuant software (version 3.0.2, AB Sciex Framingham, MA, U.S.A.). A full list of the internal standards and oxylipins is provided in Supplementary Table 4 along with limit of quantification (LOQ), calibration range, MRM transitions and corresponding MS parameters (collision energy, declustering potential). In this assay, identification is based on retention time comparison with authentic standards and the presence of a diagnostic precursor and product ion pair, however stereochemistry is not established and in the case of lower abundance lipids, is often unclear. For that reason, chirality has been removed. Limit of quantitation (LOQ) for each lipid was set at the primary standard value closest to a minimum value of 5:1 for signal:noise, and all chromatograms from tissue/cell samples were manually checked for peak quality and excluded from analysis if they fell below limit of detection (LOD) of 3:1, signal:noise. Example chromatograms for all lipids analyzed are provided in Supplementary Figure 7.

Targeted lipidomics analysis of 12(S)-HETE, 12(R)-HETE, 12(S)-HETE d8 or tetranor 12(S)-HETE metabolites was performed on a Nexera LC coupled to a 4000 QTrap (AB Sciex). Briefly, liquid chromatography was performed at 40 °C using a Spherisorb ODS2 C18 column (4.6 x 150 mm, 5 µm, Waters) at a flow rate of 1 ml/min over 30 min. Mobile

phase A was (75 % HPLC water/ 25 % acetonitrile; v/v and 0.1 % acetic acid) and mobile phase B was 60 % methanol/ 40 % acetonitrile; v/v and 0.1 % acetic acid. The following gradient for mobile phase B was applied: 50-90% B over 20 mins, then held at 90% B for 5 mins, followed by re-equilibration to 50% B from 25-30 mins. Injection volume was 10 µL. Ionization was performed using electrospray ionization in the negative ion mode with the following MS parameters: temperature 650 °C, N_2 gas, GS1 60 psi, GS2 30 psi, curtain gas 35 psi, ESI voltage -4.5 kV. Cycle time was 1.46 s. Peak areas for lipids were integrated and quantification was performed using external calibration curve with 15-HETE-d8 as standard for all investigated compounds. Data integration and quantification was performed using MultiQuant software (version 3.0.2, AB Sciex Framingham, MA, U.S.A.). MRM transitions and corresponding MS parameters (collision energy and declustering potential) for each analyzed lipid is provided in Supplementary Table 5.

Mitochondrial stress test:

Oxygen consumption rate (OCR) was measured using Seahorse XF^{e}96 analyzer (Agilent) and the Seahorse XF^{e}96 FluxPak according to the manufacturer's protocols. Briefly, RAW/RAW*Alox15* cells were seeded at 2.5 x 10^5 cells/well and peritoneal macrophages were seeded at 5 x 10^5 cells/well (and incubated with LPS (100 ng/ml). Mitochondrial function was assessed using inhibitors (all from Sigma) injected in the following order: oligomycin (1µM), FCCP (Carbonyl cyanide 4-(trifluoromethoxy)phenylhydrazone, 2 µM or 4 µM final concentration for peritoneal macrophages or RAW cells respectively), rotenone (1 µM), antimycin A (10 µM for peritoneal macrophages; 1 µM for RAW/RAW*Alox15* cells).

Heatmap method.

For generation of heatmaps, amounts (ng/10^6 cells) of each lipid were averaged, then log10 was applied to the mean value. Heatmaps were generated using Pheatmap in R. The

Euclidean metric was chosen to establish the treatments' relationships depicted as clusters[74]. The clusters are aggregated following the “shortest distance” rule. Lipids are color-coded by putative enzymatic origin (Supplementary Table 1).

Determination of reactive oxygen species generation by peripheral blood cells

Human blood from healthy workplace volunteers was obtained with ethical approval from School of Medicine (SMREC 16/02) with informed consent. Whole blood (5 ml) was drawn using a butterfly syringe into 50 μl heparin sodium; 12 μl of this was then placed in a microcentrifuge tube and 1 ml cold PBS added. Following centrifugation (350 x g, 5 min, 4 °C) the cell pellet was recovered and resuspended, then stained with anti-CD15 BV510 (1:50 in 0.5 ml PBS, W6D3, Becton Dickinson) for 30 min on ice. Cells were centrifuged (350 x g, 5 min, 4 °C) and resuspended in DMEM media (+2 mM glutamine) containing amino-phenyl fluorescein (APF) (1:1000, cell concentration = cells from 5 µl blood per ml of APF media). S. epidermidis bacteria (clinical isolate)[44] were killed by incubation at 65 °C for 20 min, then washed by centrifugation and resuspended in PBS three times (12,000 x g, 5 min). Bacteria were counted by flow cytometry using an Attune NXT; bacteria were excluded from other particles by size (Forward-scatter vs Side-scatter). Bacteria were first added to blood cells at varying doses, to determine optimal reactivity per donor isolate (ranging from 1.37×10^5 - 2.75×10^6 bacteria per ml of APF media containing cells from 5 µl blood). For this, cells+bacteria were incubated for 20 min at 37 °C, then tubes place on ice. Cells were washed three times with ACK red blood cell lysing buffer (350 x g, 5 min, 4 °C) then analyzed by flow cytometry. Cell gating strategies are shown in Supplementary Figure 6 C-E. This included forward- vs side-scatter profile (FSC vs SSC) that distinguishes neutrophils and monocytes from lymphocytes. Neutrophils were further separated from eosinophils and monocytes via their high expression of CD15 (Supplementary Figure 2 C-E). The bacterial dose was selected based on a neutrophil APF^+ response of between 10 -

40 % APF^{+ve} cells. Once this was optimized, the experiment was repeated in triplicate for each donor, and using three individual donors, using a fresh aliquot of blood. The additional step following APF addition, was that lipids or ethanol vehicle (1:100) were added and samples incubated at 37 °C for 10 min before the bacteria addition step. Lipids used and final concentrations are provided in Supplementary Table 2. Calculations assumed a 100 µl peritoneal volume *in vivo* (Supplementary Table 2) [75]. Next, bacteria were added, cells were incubated for 20 min at 37 °C, then tubes place on ice, washed, and analyzed using flow cytometry for APF^{+ve} neutrophils or monocytes. Means for each donor were calculated separately and compared using two-way ANOVA with Sidaks post-test, where $p < 0.05$ was considered significant.

Assessment of mitochondrial DNA in LPS treated cells

RAW cells were seeded in 6 well plates at a density of $1x10^6$ cells/well and grown in DMEM (Lonza), supplemented with 10% FCS (Thermo Fisher Scientific), 2mM glutamine (Lonza) and 100 U/ml of penicillin/streptomycin (Lonza), 24 h prior to treatment. After 24 hrs, the medium was aspirated, and cells treated with LPS (100 ng/ml) or chloroquine (40 nM) and incubated for 24 hours. Total DNA was extracted from cells with PureLink Genomic DNA kit (Fisher Scientific, cat. No. 10053293) according to the manufacturer's instructions and quantified using a Nanodrop (Thermo Scientific). Assessment of mtDNA copy numbers, relative to genomic DNA (gDNA), was done as previously described (PMID: 29677567). Briefly, quantitative PCR (qPCR) analysis was performed using PerfeCta™ SYBR® Green FastMix™, low ROX™ (Quanta Biosciences) and primers specific for mouse mtDNA (mouse mtDNA forward: 5'-CCCCAGCCATAACACAGTATCAAAC-3', mouse mtDNA reverse: 5'- GCCCAAAGAATCAGAACAGATGC-3') or the genomic 18S ribosome gene (mouse 18S forward: 5'- AAACGGCTACCACATCCAAG-3', mouse 18S reverse: CAATTACAGGGCCTCGAAAG-3') (Merck KGaA). Primers specific for mtDNA gives rise to

a 201bp product, while primers specific for the 18S ribosomal gene gives a product that is 112 bp large. Quantitative PCR analysis was performed in a Stratagene MX3000P machine (Stratagene California, San Diego, CA, USA) using 96-well Non-Skirted, White PCR Plates (ABgene, UK) and MicroAmp Optical Caps (Applied Biosystems, UK). For qPCR, each sample reaction was performed on 25 ng of diluted total DNA in a total reaction volume of 20 μL, under the following conditions: 95°C for 2 minutes; 95°C for 15 seconds, 60°C for 1 minute, repeated 40 cycles; 95 °C for 1 minute, 55 °C for 30 s, 95°C for 30 s. To assess the mtDNA copy numbers, the ratio of mtDNA/gDNA was generated by normalizing the quantified mtDNA values to the quantified 18S DNA values.

To calculate mtDNA damage based on Lesion frequency, the DNA of the cells was isolated as described above and Assessment of mtDNA damage was done as previously described (PMID: 29677567). Using quantitative PCR (qPCR) analysis s describe above. A common reverse primer used (mouse mtDNA reverse: 5'-GCCCAAAGAATCAGAACAGATGC-3') in combination with a forward primer called, short PCR primer (mouse short PCR primer 5'-GCAAATCCATATTCATCCTTCTCAAC-3') or a forward primer called forward long PCR primer (long PCR primer 5'-CCCAGCTACTACCATCATTCAAGTAG-3'). The reverse primer with the short forward primer gives rise to a 16.2 kb product, while in combination with the long PCR primer give rise to a 80 bp product. The lesion frequency of the mtDNA s calculate using the equation below [76].

$$\text{Lesion Frequency per 16kb} = -Ln\left(\frac{Long\ PCR\ product/Short\ PCR\ product}{mean\ of\ (Long\ PCR\ product/Short\ OCR\ product)\ from\ control}\right.$$

Table 1 mtDNA primers for copy number assessment					
Assay	Species	Target	Direction	Sequence	product
mtDNA copy number	Mouse	18s Ribosome	Forward	AAACGGCTACCACATCCAAG	112 bp
	Mouse	18s Ribosome	Reverse	CAATTACAGGGCCTCGAAAG	
	Mouse	mouse mtDNA	Forward	CCCCAGCCATAACACAGTATCAAAC	201 bp
	Mouse	mouse mtDNA	Reverse	GCCCAAAGAATCAGAACAGATGC	
mtDNA Damage	Mouse	mouse mtDNA	Forward short primer (short PCR product)	GCAAATCCATATTCATCCTTCTCAAC	80 bp
	Mouse	mouse mtDNA	Forward long	CCCAGCTACTACCATCATTCAAGTAG	16.2 kb

			primer (long PCR product)		

Transcriptional analysis of GEO datasets.

A set of genes relevant to mitochondrial β-oxidation were collated, and then examined for differential gene expression (Supplementary Table 3). Published transcriptome data (NCBI Geo DataSets Accession numbers GSE53053; GSE69607; GSE84517; GSE46903; GSE35449 and GSE5099) regarding different macrophage phenotypes (M0 or M1 from both murine and human origin) generated using similar experimental conditions to those in the current study, were downloaded. All datasets were processed in R and using packages from Bioconductor. Affymetrix microarray data (GSE69607, GSE5099) were normalized and processed using Limma and Oligo Bioconductor packages[77, 78]. Illumina beadchip microarray data (GSE46903, GSE35449) were normalized and processed using Limma and lumi Bioconductor packages [77, 79]. Paired-end reads from Illumina sequencing (GSE53053, GSE84517) were trimmed with Trim Galore and assessed for quality using FastQC, using default parameters [80, 81]. Reads were mapped to the reference sequence (human GRCh38 or mouse GRCm38) reference genome using STAR and counts were assigned to transcripts using featureCounts with the Ensembl gene build GTF (GRCh38.96 or GRCm38.84)[82, 83]. Both the reference genome and GTF were downloaded from the Ensembl FTP site (http://www.ensembl.org/info/data/ftp/index.html/). Differential gene expression analyses used the DESeq2 package[84]. Genes were discarded from the analysis differential expression failed to be significant (significance: adj.pval < 0.05, Benjamini-Hochberg correction for multiple testing).

Analysis of human microarray data.

Data from a published study was obtained[45]. Here, whole blood was analyzed using Illumina Human Whole-Genome Expression BeadChip HT12v3 microarrays comprising

48,802 features (human gene probes) from neonates with proven microbiological evidence of infection from a usually sterile body site (35 controls, 26 bacterial confirmed sepsis cases). These patients also demonstrated significantly elevated expression markers which form part of the published classifier for sepsis[45]. Log2 expression data for the set of relevant genes (Supplementary Table 3) was compared, Students t-test, significance: adj.pval < 0.05, Benjamini-Hochberg correction for multiple testing.

Analysis of mouse in vivo bacterial peritonitis gene expression

The SES model was carried out and lavage harvested at 3 or 6 hrs as described[46]. 8-12 weeks old WT C57Bl/6 mice were from Charles River. C57Bl/6 interleukin-6 ($Il6^{-/-}$) mice were bred in house (UK Home Office PPL 30/2938, PPL P05D6A456). Parietal peritoneal tissue was extracted at 3 and 6 h post SES administration, collected using aseptic techniques. Two sections of lining were immediately snap frozen in liquid N_2 and stored at -80 ºC prior to total RNA extraction. For this, peritoneal membrane sections (80 mg) were dissociated in 1 ml buffer RLT (QIAGEN) supplemented with β-mercaptoethanol (1:100 v:v) using a handheld electric homogenizer (Benchmark Scientific). Lysate was diluted 1:3 in distilled water and digested in 0.2 mg/ml proteinase-K (Invitrogen; 25530049) for 10 min at 55 ºC. Lysate was cleared and RNA precipitated in 70 % ethanol. Total RNA was extracted using the RNeasy minikit (QIAGEN; 24136) in accordance with the manufacturer's instructions. RNA was eluted in 50 µl RNase-free water and quantified using a nanodrop 2000. The integrity and quality of RNA preparations was assessed using an Agilent 2100 bioanalyzer. Samples with an RNA integrity number (RIN) exceeding 8 were used for library preparation (2-4 µg input). Cytoplasmic, mitochondrial, and ribosomal RNA was depleted using the Ribominus transcriptome isolation kit (Ambion; K155001). Libraries were prepared using the RNA-seq kit v2 (Life technologies; 4475936) and sequencing on an ion torrent (Thermo Fisher). Raw data was mapped using Torrent Suite™ (STAR and Bowie2

aligners) using mm10 as the reference genome. Library quality was assessed using FastQC (Babraham Institute) and Github. Differential gene expression analysis was completed with DEseq2 (Bioconductor). For the specific genes tested (Supplementary Table 3), Students t-test was used, significance: adj.pval < 0.05, Benjamini-Hochberg correction for multiple testing.

Acknowledgements. Funding from Wellcome Trust (094143/Z/10/Z) and European Research Foundation (LipidArrays) is gratefully acknowledged (VBO). VBO is a Royal Society Wolfson Research Merit Award Holder and acknowledges funding for LIPID MAPS from Wellcome Trust (203014/Z/16/Z). Ser Cymru Project Sepsis grant funded by WG/EU-ERDF (PG, VBO). PRT is funded by a Wellcome Trust Investigator Award (107964/Z/15/Z) and the UK Dementia Research Institute. VDU acknowledges The Nathan Shock Center P30 AG05088. Kidney Research UK (Reference RP-024-20160304 awarded to SAJ), Versus Arthritis (Reference 20770 awarded to SAJ, VOD). We gratefully acknowledge expert input from Alan Brash, Vanderbilt University, relating to lipid structural elucidation, James Burston for supporting analysis of mitochondrial function, Widad Dantoft for provision of the human sepsis dataset, and our colleague Javier Uceda Fernandez (deceased), Cardiff University for the murine transcriptomics dataset.

Figure legends:

Figure 1. Inhibition of CPT1 increases oxylipin levels significantly during inflammation *in vivo*. Wild type mice (female, 7-9 weeks) were injected ip with vehicle (PBS), etomoxir (100 μg) or LPS (1 μg). After 6 hrs, lavage was harvested and lipids extracted using SPE then analyzed using LC/MS/MS as outlined in Methods. *Panel A.*

Lipidomics reveals the impact of CPT1 on oxylipin metabolism. A heatmap was generated using Pheatmap as described in Methods, with data as log10 ng/total mouse lavage for all oxylipins (n = 10, * p<0.05, Students T-test, black: significant elevation, green: significant reduction). *Panel B. Box and whisker plots for individual lipids showing that inhibition of CPT1 enhances oxylipin levels, with a bigger impact during inflammatory challenge with LPS*. A series of example lipids from 12/15-LOX, COX and CYP450 are shown (n = 10, * p < 0.05, ** p< 0.01, *** p < 0.005, Students T-test, for with/without etomoxir), outliers are shown in red.

Figure 2. Inhibition of CPT1 increases oxylipin secretion significantly during inflammation in peritoneal macrophages. Peritoneal macrophages were isolated as described in Methods, then cultured in serum-free medium in the presence of etomoxir (25 μM) with/without LPS (100 ng/ml). After 24 hrs, supernatant was harvested and lipids extracted using SPE, then analyzed using LC/MS/MS. *Panel A. Heatmap shows that many lipids are elevated when CPT1 is inhibited*. A heatmap was generated using Pheatmap as described in Methods, with data as log10 ng/10^6 for all oxylipins (n = 3, * p<0.05, Students T-test, black: significant elevation, green: significant reduction). *Panels B-E Bar charts for individual lipids showing impact of etomoxir +/- LPS on oxylipin release by peritoneal macrophages in vitro.* A series of lipids based on enzymatic origin are shown, n = 3 per sample, mean +/- SEM, * p < 0.05, ** p< 0.01, *** p < 0.005, Students T-test, for with/without etomoxir.

Figure 3. Bone marrow derived M0, M1 and M2 cells consume diverse oxylipins from serum, and M1 cells consume prostaglandins via CPT1. *Panels A-C. Serum derived mono-hydroxy oxylipins are metabolized by M0, M1 and M2 cells.* BMDM-derived M0, M1, and M2 cells were derived during a 24 hr culture in medium containing 10 % FCS, as

described in Methods, then supernatant extracted and analyzed for mono-hydroxy oxylipins using LC/MS/MS as described in Methods (n = 3, mean +/- SEM. * $p < 0.05$, ** $p < 0.01$, *** $p < 0.005$, Students T test, cells *versus* media). *Panels D,E. M1 cells robustly generate prostaglandins and related oxylipins, that are low abundance in serum*. BMDM-derived cells were treated as in Panel A, and supernatants analyzed for prostaglandins. (n = 3, mean +/- SEM). *Panel F. M1 cell secretion of prostaglandins is increased by CPT1 inhibition*. BMDM-derived M1 cells were treated in the absence (control) or presence (etomoxir) of etomoxir (25 μM) for 24hr. Here, FCS-free medium was used to avoid contaminating oxylipins from serum (n = 3, mean +/- SEM. * $p < 0.05$, *** $p < 0.005$ with/without etomoxir, Students T test).

Figure 4. Inhibition of CPT1 increases secretion of 12/15-LOX-derived eicosanoids from RAW cells overexpressing *Alox15*. *Panel A. A heatmap was generated using Pheatmap as described in Methods*. Raw^{mock} and Raw*Alox12* cells were cultured with etomoxir (25 μM) and/or LPS (100 ng/ml) for 24 hr before harvest and SPE extraction of supernatant for oxylipin analysis using LC/MS/MS. Data are shown as log10 ng/10^6 values for all oxylipins. (n = 6, * $p < 0.05$, Students T test, black: significant elevation, green: significant reduction). *Panels B-F. Blockade of CPT1 leads to significant elevation of 12/15-LOX-derived oxylipins in Raw cells*. Bar charts showing how oxylipins from 12/15-LOX are impacted by etomoxir (n = 6, mean +/- SEM). *Panels G-H. Etomoxir reduces secretion of COX-2 derived oxylipins in RAW cells* (n = 6, mean +/- SEM). * $p < 0.05$, ** $p < 0.01$, *** $p < 0.005$ for with/without etomoxir, Students T test.

Figure 5. RAW cells rapidly consume exogenous 12-HETE, secreting two tetranor metabolites which are then rapidly metabolized by mitochondrial β-oxidation. *Panel A. 12-HETE is rapidly consumed and converted to two tetranor 12-HETE metabolites by RAW*

cells. RAW cells were cultured for up to 12 hr in serum free medium with 1.4 μg 12(S)-HETE added per 10^6 cells. At varying timepoints, samples were harvested and lipids extracted and analyzed using LC/MS/MS as described in Methods. *Panels D-I. CPT1 inhibition prevents metabolism of 12(S), 12(R)-HETEs and their tetranor triene and diene metabolites*. *Panels D,F,H. Etomoxir prevents metabolism of 12(S)-HETE and its metabolites.* Cells were supplemented with 1.5 μg 12(S)-HETE/10^6 cells were added for 3 hrs with/without etomoxir (25 μM), then supernatants and cells were analyzed for levels of 12-HETE and its triene and diene tetranor products. *Panels E,G,I. Etomoxir prevents metabolism of 12(R)-HETE and its metabolites.* Cells were supplemented with 1.5 μg 12(R)-HETE/10^6 cells for 3 hrs with/without etomoxir (25 μM), then supernatants and cells were analyzed for levels of 12-HETE and its triene and diene tetranor products (n = 4, mean +/- SEM. * $p < 0.05$, *** $p < 0.005$ with/without etomoxir, Students T test).

Figure 6. CPT1 genetic knockdown reduces secretion of prostaglandins and 17,18-diHETE,

Panels A-D Cpt1a knockdown prevents secretion of PGs from RAW cells. RAW cells expressing either the non-silencing (RAW^{nonsil}) or Cpt1a knockdown siRNA ($RAW\mathit{Cpt1a}^{KD}$) were treated with LPS (100 ng/ml) for 24 hr and secretion of PGs, 17,18-diHETE or monohydroxy oxylipins measured using LC/MS/MS as in methods. (n = 6, mean +/- SEM) *** $p < 0.005$ control vs knockdown, Students T test. *Panel E-G Cpt1a knockdown impacts on removal of 12-HETE and secreted levels of tetranor diene and triene metabolites by RAW cells*. RAW cells were incubated +/- LPS (100 ng/ml, for 4 hr) with 12-HETE (2.34 μg/ml) added after the first hour (thus added for 3 hr). Supernatants and cells were harvested, then lipids extracted and analyzed for 12-HETE and metabolites using LC/MS/MS as described in Methods. Data (n = 5 - 6 per group) represents two independent experiments.

Figure 7. CPT1 inhibition reduces metabolism of tetranor triene 12-HETE *in vivo*, OxPhos is suppressed in LPS-stimulated macrophages and *in vivo* amounts of oxylipins promote neutrophil ROS generation. *Panel A. Tetranor triene 12-HETE is increased in vivo during inflammation with CPT1 inhibition.* Wild type mice (female, 7-9 weeks) were injected ip with vehicle (PBS), etomoxir (100 μg) and/or LPS (1 μg). After 6 hrs, lavage was harvested and lipids extracted and analyzed using LC/MS/MS as outlined in Methods (n = 10, * $p < 0.05$, ** $p < 0.01$, *** $p < 0.005$, Students T-test, for with/without etomoxir). Outliers are shown as red, or with values. *Panel B. LPS treatment of RAW or naïve peritoneal macrophages reduces mitochondrial OxPhos*. RAW, RAW*Alox15*, or naïve peritoneal macrophages from wild type or *Alox15*$^{-/-}$ mice were treated with LPS (100 ng/ml) for 24 hrs. Mitochondrial function was assessed as described in Methods (n = 3-6 mean +/- SEM). *Panels C,D. LPS doesn't alter mitochondrial DNA or lesion frequency in RAW macrophages.* RAW and RAW*Alox15* cells were mock treated or treated with CQ (40 nM) or LPS (100 ng/ml) for 24 hr. Subsequently their DNA was isolated and used to assess the mtDNA to gDNA ratio (C) and the frequency of lesions in mtDNA (D) using qPCR (three independent experiments with n = 3, one-way ANOVA with Tukeys correction, no data were significantly different from RAW samples, except RAW+CQ, as expected for lesion frequency only, acting as a positive control). *Panels E-H Oxylipin levels detected in vivo promote neutrophil ROS generation.* Whole blood was incubated with oxylipin mixtures (Supplementary Table 2), and then ROS generation in response to stimulation using opsonized *S. epidermidis* determined by APF fluorescence as indicated in Methods. Three individual donor samples were separately tested in triplicate. Monocytes and neutrophils were analyzed using gating strategy as outlined in Methods. *Panels E,F. Response to high or low oxylipin doses were expressed either as %APF+ cells or %increase over the vehicle (ethanol) response*. The average value from each donor is

shown separately. *Panels G,H Bar chart for one representative donor, showing comparison with unstimulated blood.* Neutrophils (C), monocytes (D) (n = 3, mean +/- SEM). Data was analyzed by two-way ANOVA with Sidaks post hoc tests indicated (* = P<0.05, ** = P<0.01, *** = P<0.001). ANOVA values were (*E* – pairing P <0.001, cell type P=0.018, lipid and interaction P<0.001; *F* – pairing P <0.001, cell type P=0.009, lipid P=0.008 and interaction P=0.002; *G* – interaction, bacteria and lipid P<0.001; *H* – interaction P=0.47, bacteria P<0.001, lipid P=0.39). Data shows the mean average numbers from one donor but represents the results from three donors from two independent experiments.

Figure 8. Graphic showing formation and mitochondrial metabolism of oxylipins.

Figure 9. Transcriptomics of human neonatal sepsis and mouse bacterial peritonitis proposes multiple genes that support a mitochondrial oxylipin β-oxidation pathway. *Panel A. Human transcriptomics data shows significant upregulation of several genes including ACSL and CPT isoforms.* Gene expression (log2 expression data) from 35 controls and 26 bacterial confirmed sepsis cases published in [45] were compared for expression of 32 genes putatively involved in import and β-oxidation of oxylipins, based on known metabolic pathways for long chain native FA. Raw data are provided in Supplementary Table 6. *Panel B. Box and whisker plots for the 8 significantly upregulated genes are shown.* n = 35 and 26 for infection and controls, respectively. * p < 0.05, *** p < 0.005, Students T-test, then adjusted using Benjamini-Hochberg test. *Panel C. Transcriptomics of mouse peritonitis shows significant upregulation of Cpt1a at 6 hrs*. Gene expression data from peritoneal membranes harvested post SES challenge was analyzed for expression of 32 genes as for Panel A, above (n = 3 per group) * p < 0.05, Students T-test, adjusted using Benjamini-Hochberg test.

Figure 10. Transcriptomics of the mitochondrial β-oxidation pathway reveals *ACSL1/Acsl1* as a key checkpoint response to LPS inflammation in human and mouse macrophages. *Panels A,B. Transcriptomics reveals Ascl1 to be highly upregulated in response to LPS/IFNγ in murine BMDM.* Transcriptomics data obtained from GEO database was analyzed as outlined in Methods for expression of 34 genes selected for potential or known involvement in mitochondrial β-oxidation. Samples were BMDM treated with either LPS/IFNγ or IFNγ alone as indicated. For all genes, the log2fold change was calculated and plotted using Pheatmap in R. Panel C shows box and whisker plots for normalized expression of *Acsl1* in the mouse datasets, with n = 3 for all groups except for GSE53053 M0 (n = 2) *** $p < 0.005$, Students T-test, then adjusted using Benjamini-Hochberg test. *Panel D. ACSL1 is strongly induced in human M1 macrophages.* Human transcriptomics data for ACSL1 expression was downloaded from GEO and normalized expression level plotted (n = 3-12 per group). * $p < 0.05$, *** $p < 0.005$, Students T-test.

Scheme 1. Proposed MS/MS for 8S-hydroxy-4Z,6E,10Z-hexadecatrienoic acid.

Scheme 2. Proposed MS/MS for 8S-hydroxy-6E,10Z-hexadecadienoic acid.

Scheme 3. Proposed MS/MS for D_6-8S-hydroxy-6E,10Z-hexadecadienoic acid.

Scheme 4. Proposed biochemical mechanism of β-oxidation for 12-HETE.

Supplementary Figure 1. LC/MS/MS of "Mar1" in mouse peritonitis in response to LPS, and the impact of CPT1 inhibition on oxylipins in naïve peritoneal and RAW macrophages *in vitro*, representative chromatograms for "RvD5" in RAWAlox15 cells. *Panel A. LC/MS/MS of lipid extract from peritoneal lavage (mouse treated with etomoxir and LPS)***.** A lipid with same retention time as Mar1 was detected in lavage from mice treated with etomoxir and LPS *in vivo*, labelled herein as 7,14-diHDOHE, standard is shown in left

panel, mouse lipid in right panel. *Panels B-D. The impact of LPS and etomoxir on generation of various oxylipins, measured by LC/MS/MS, in wild type and Alox15$^{-/-}$ (KO) naïve peritoneal macrophages*. Supernatant from peritoneal macrophages was analyzed for oxylipins following culture of macrophages as outlined in methods, for 24 hrs with LPS (100 ng/ml) +/- etomoxir (25 μM). *Panel E. Supernatant from RAWAlox15 cells treated with LPS/etomoxir contains isomers of 7,17-di-HDOHE*. Cells were cultured with LPS/etomoxir for 24 hrs as in Methods, then supernatant was analyzed for the presence of RvD5 using LC/MS/MS/MS (lower panel). Authentic standard is shown for comparison (upper panel). *Panel F. Etomoxir reduces generation of 17,18-diHETE from RAW cells*. RAW cells were cultured for 24 hr with/without etomoxir (dose) and LPS (dose) before supernatant was harvested and analyzed using LC/MS/MS as in Methods. (n = 6, mean +/- SEM). *** $p < 0.005$ for with/without etomoxir, Students T test.

Supplementary Figure 2. Mass spectrometry confirmation of formation of two tetranor 12-HETE metabolites in RAW cells. 12(S)-HETE or 12-HETE-d8 (2.8 μg) were incubated with RAW cells for 3 hrs and then supernatants harvested for LC/MS/MS. *Panels A,B. Formation of tetranor diene and triene 12-HETEs.* A representative sample is shown for each, including chromatogram and MS/MS spectrum, with control (dotted line) and 12(S)-HETE-supplemented (solid line) samples overlaid. *Panel C. MS/MS of the tetranor triene 12-HETE standard*. *Panels D,E. Formation of the 12(S)-HETE-d8 tetranor diene, following supplementation of 12(S)-HETE-d8 to RAW cells,* showing a representative chromatogram (D) and MS/MS spectrum (E).

Supplementary Figure 3. High resolution MS/MS of the 12-HETE tetranor triene standard and tetranor triene 12(S)-HETE is converted into the diene isomer in macrophages. *Panel A.* Extracted Ion chromatogram, high resolution MS spectrum, and

MS/MS spectrum of the tetranor-12(S)-HETE triene standard. *Panel B. Addition of tetranor triene 12(S)-HETE leads to formation and secretion of the diene isomer*. 2.8 μg triene standard was incubated with 10^6 RAW cells for 3 hr, then supernatants harvested and analyzed using LC/MS/MS.

Supplementary Figure 4. ^{1}H and ^{1}H-^{1}H COSY NMR spectra of the tetranor-12(S)-HETE standard. *^{1}H (Panel A) and ^{1}H-^{1}H COSY (Panel B) NMR* demonstrates that the H11 vinyl proton at 5.60 ppm is connected to the methylene H12 protons at 2.05 ppm, which itself is connected back to the alkyl protons at 1.33 ppm. This identifies the 5.60 ppm signal as H11, which correlates with one of the protons that overlap at 5.4 ppm (area of two protons). This 5.4 ppm signal must then be the H10 proton as well as the H4 vinyl proton (which correlates with the H5 vinyl proton and H3 methylene protons).

Supplementary Figure 5. *Panel A. Images of RAW264 cells infected with viruses* (purified by 2.5 μg/ml puromycin) taken on a 10x objective lens using an EVOS microscope (Life Technologies). Image shows transmitted brightfield overlaid with Green fluorescent GFP. *Panel B. Representative images showing GFP expression and sort gates for RAW264 cells infected with viruses using the BD FACS Aria II flow cytometer*. *Panel C. Cpt1a expression is suppressed in Cpt1a^{KD} cells versus Cpt1a^{null}.* Bar graph showing the effect of Cpt1a knockdown shRNA on Cpt1a gene expression in RAW264 macrophages. Data was recorded by measured by real-time PCR. Data (n = 3 per group) represents at least two independent experiments related to Figure 6. *Panel D. Expression of Alox15 in RAW cells.* RNA was isolated from the RAW*Alox15$^{-/-}$* and pMX-IP control cell lines, then converted to cDNA and PCR was performed using primers to amplify *Alox15*. Amplified PCR products were run on a 10% agarose gel and showed that *Alox15* was amplified from the *Alox15* plasmid, but not from the pMX-IP cDNA (plasmid) control, or the no DNA (no plasmid)

control, thereby confirming expression as expected. Chromatogram shows generation of 12-HETE in RAWAlox15 cells only, but not mock transfected controls.

Supplementary Figure 6. Confirmation of phenotype in bone marrow derived macrophages. *Panel A*. *M1 macrophages secrete typical cytokines*. Cytokine production of typical M1 phenotype markers (IL-65, CCL5 and TNF) were determined by ELISA analyses of supernatants post differentiation as described in Methods. *Panel B. Confirmation of classical and alternative activation in BMDM*. RNA was isolated from activated BMDM, converted to cDNA and then analyzed by real time PCR as described in Methods section. Probes for typical phenotype markers are indicated inset, mean +/- SD. *Panels C-E. APF flow cytometric gating strategy.* Representative flow cytometry plots showing the gating strategy for neutrophils and monocytic cells, with a distinctive forward- vs side-scatter profile (FSC vs SSC) that distinguishes them from lymphocytes (Panel C). Neutrophils were further distinguished from eosinophils and monocytes via high expression of CD15. Representative gating for Aminophenyl fluorescein (APF) positive neutrophils (Panel D) and monocytes (Panel E) is depicted in the presence or absence of *Staphylococcus epidermidis* (*S. epi*).

Supplementary Figure 7. **Representative chromatograms from oxylipin analysis showing typical peaks detected.**

References

1. Funk, C.D., *Prostaglandins and leukotrienes: advances in eicosanoid biology.* Science, 2001. **294**(5548): p. 1871-5.
2. Simmons, D.L., R.M. Botting, and T. Hla, *Cyclooxygenase isozymes: the biology of prostaglandin synthesis and inhibition.* Pharmacol Rev, 2004. **56**(3): p. 387-437.

3. Smith, W.L., D.L. DeWitt, and R.M. Garavito, *Cyclooxygenases: structural, cellular, and molecular biology.* Annu Rev Biochem, 2000. **69**: p. 145-82.

4. Serhan, C.N., N. Chiang, and T.E. Van Dyke, *Resolving inflammation: dual anti-inflammatory and pro-resolution lipid mediators.* Nat Rev Immunol, 2008. **8**(5): p. 349-61.

5. Capdevila, J.H., J.R. Falck, and J.D. Imig, *Roles of the cytochrome P450 arachidonic acid monooxygenases in the control of systemic blood pressure and experimental hypertension.* Kidney Int, 2007. **72**(6): p. 683-9.

6. Fleming, I., *DiscrEET regulators of homeostasis: epoxyeicosatrienoic acids, cytochrome P450 epoxygenases and vascular inflammation.* Trends Pharmacol Sci, 2007. **28**(9): p. 448-52.

7. Imig, J.D., *Targeting epoxides for organ damage in hypertension.* J Cardiovasc Pharmacol, 2010. **56**(4): p. 329-35.

8. Roman, R.J., *P-450 metabolites of arachidonic acid in the control of cardiovascular function.* Physiol Rev, 2002. **82**(1): p. 131-85.

9. Spector, A.A. and A.W. Norris, *Action of epoxyeicosatrienoic acids on cellular function.* Am J Physiol Cell Physiol, 2007. **292**(3): p. C996-1012.

10. Williams, J.M., et al., *20-hydroxyeicosatetraeonic acid: a new target for the treatment of hypertension.* J Cardiovasc Pharmacol, 2010. **56**(4): p. 336-44.

11. Breyer, R.M., et al., *Prostanoid receptors: subtypes and signaling.* Annu Rev Pharmacol Toxicol, 2001. **41**: p. 661-90.

12. Cheng, H.F. and R.C. Harris, *Cyclooxygenases, the kidney, and hypertension.* Hypertension, 2004. **43**(3): p. 525-30.

13. Hao, C.M. and M.D. Breyer, *Physiological regulation of prostaglandins in the kidney.* Annu Rev Physiol, 2008. **70**: p. 357-77.

14. Capra, V., et al., *Cysteinyl-leukotrienes and their receptors in asthma and other inflammatory diseases: critical update and emerging trends.* Med Res Rev, 2007. **27**(4): p. 469-527.

15. Ribeiro, J.D., A.A. Toro, and E.C. Baracat, *Antileukotrienes in the treatment of asthma and allergic rhinitis.* J Pediatr (Rio J), 2006. **82**(5 Suppl): p. S213-21.

16. Sharma, J.N. and L.A. Mohammed, *The role of leukotrienes in the pathophysiology of inflammatory disorders: is there a case for revisiting leukotrienes as therapeutic targets?* Inflammopharmacology, 2006. **14**(1-2): p. 10-6.

17. Diczfalusy, U., et al., *Metabolism of prostaglandin F2 alpha in Zellweger syndrome. Peroxisomal beta-oxidation is a major importance for in vivo degradation of prostaglandins in humans.* J Clin Invest, 1991. **88**(3): p. 978-84.

18. Wigren, J., et al., *Metabolism of 12(S)-hydroxy-5,8,10,14-eicosatetraenoic acid by kidney and liver peroxisomes.* J Lipid Res, 1993. **34**(4): p. 625-31.

19. Diczfalusy, U., *Beta-oxidation of eicosanoids.* Prog Lipid Res, 1994. **33**(4): p. 403-28.

20. Spector, A.A., J.A. Gordon, and S.A. Moore, *Hydroxyeicosatetraenoic acids (HETEs).* Prog Lipid Res, 1988. **27**(4): p. 271-323.

21. Benedetto, C., McDonald-Gibson, R.G., Nigam, S., Slater, T.F. , *Prostaglandins and Related Substances: A Practical Approach*. 1988, Oxford, Washington, 1987: IRL Press.

22. Eaton, S., K. Bartlett, and M. Pourfarzam, *Mammalian mitochondrial beta-oxidation.* Biochem J, 1996. **320 (Pt 2)**: p. 345-57.

23. Wang, H.Y. and H. Schulz, *Beta-oxidation of polyunsaturated fatty acids with conjugated double bonds. Mitochondrial metabolism of octa-2,4,6-trienoic acid.* Biochem J, 1989. **264**(1): p. 47-52.

24. Houten, S.M., et al., *The Biochemistry and Physiology of Mitochondrial Fatty Acid beta-Oxidation and Its Genetic Disorders.* Annu Rev Physiol, 2016. **78**: p. 23-44.

25. Kaminski, M.M., et al., *Polarization and asymmetry in T cell metabolism.* Semin Immunol, 2016. **28**(5): p. 525-534.

26. O'Neill, L.A. and E.J. Pearce, *Immunometabolism governs dendritic cell and macrophage function.* J Exp Med, 2016. **213**(1): p. 15-23.

27. Slatter, D.A., et al., *Mapping the Human Platelet Lipidome Reveals Cytosolic Phospholipase A2 as a Regulator of Mitochondrial Bioenergetics during Activation.* Cell Metab, 2016. **23**(5): p. 930-44.

28. Palmieri, E.M., et al., *Nitric oxide orchestrates metabolic rewiring in M1 macrophages by targeting aconitase 2 and pyruvate dehydrogenase.* Nature Communications, 2020. **11**(1): p. 698.

29. O'Neill, L.A., R.J. Kishton, and J. Rathmell, *A guide to immunometabolism for immunologists.* Nat Rev Immunol, 2016. **16**(9): p. 553-65.

30. Thapa, B. and K. Lee, *Metabolic influence on macrophage polarization and pathogenesis.* BMB Rep, 2019. **52**(6): p. 360-372.

31. Bennett, M.J. and A.B. Santani, *Carnitine Palmitoyltransferase 1A Deficiency*, in *GeneReviews((R))*, M.P. Adam, et al., Editors. 1993: Seattle (WA).

32. Gessner, B.D., et al., *Evidence for an association between infant mortality and a carnitine palmitoyltransferase 1A genetic variant.* Pediatrics, 2010. **126**(5): p. 945-51.

33. Sinclair, G., et al., *The p.P479L variant in CPT1A is associated with infectious disease in a BC First Nation.* Paediatr Child Health, 2019. **24**(2): p. e111-e115.

34. Dioszeghy, V., et al., *12/15-Lipoxygenase regulates the inflammatory response to bacterial products in vivo.* J Immunol, 2008. **181**(9): p. 6514-24.

35. Cornicelli, J.A., et al., *Mouse peritoneal macrophages contain abundant omega-6 lipoxygenase activity that is independent of interleukin-4.* Arterioscler Thromb Vasc Biol, 1996. **16**(12): p. 1488-94.

36. Murray, P.J., et al., *Macrophage activation and polarization: nomenclature and experimental guidelines.* Immunity, 2014. **41**(1): p. 14-20.

37. Kriska, T., et al., *Deactivation of 12(S)-HETE through (omega-1)-hydroxylation and beta-oxidation in alternatively activated macrophages.* J Lipid Res, 2018. **59**(4): p. 615-624.

38. Divakaruni, A.S., et al., *Etomoxir Inhibits Macrophage Polarization by Disrupting CoA Homeostasis.* Cell Metab, 2018. **28**(3): p. 490-503 e7.

39. Raud, B., et al., *Etomoxir Actions on Regulatory and Memory T Cells Are Independent of Cpt1a-Mediated Fatty Acid Oxidation.* Cell Metab, 2018. **28**(3): p. 504-515 e7.

40. Yao, C.-H., et al., *Identifying off-target effects of etomoxir reveals that carnitine palmitoyltransferase I is essential for cancer cell proliferation independent of β-oxidation.* PLOS Biology, 2018. **16**(3): p. e2003782.

41. Zhang, J., F.E. Frerman, and J.J. Kim, *Structure of electron transfer flavoprotein-ubiquinone oxidoreductase and electron transfer to the mitochondrial ubiquinone pool.* Proc Natl Acad Sci U S A, 2006. **103**(44): p. 16212-7.

42. Jha, A.K., et al., *Network integration of parallel metabolic and transcriptional data reveals metabolic modules that regulate macrophage polarization.* Immunity, 2015. **42**(3): p. 419-30.

43. Ryan, D.G. and L.A.J. O'Neill, *Krebs cycle rewired for macrophage and dendritic cell effector functions.* FEBS Lett, 2017. **591**(19): p. 2992-3006.

44. Hurst, S.M., et al., *Il-6 and its soluble receptor orchestrate a temporal switch in the pattern of leukocyte recruitment seen during acute inflammation.* Immunity, 2001. **14**(6): p. 705-14.

45. Smith, C.L., et al., *Identification of a human neonatal immune-metabolic network associated with bacterial infection.* Nat Commun, 2014. **5**: p. 4649.

46. Fielding, C.A., et al., *Interleukin-6 signaling drives fibrosis in unresolved inflammation.* Immunity, 2014. **40**(1): p. 40-50.

47. Beyer, M., et al., *High-resolution transcriptome of human macrophages.* PLoS One, 2012. **7**(9): p. e45466.

48. Huang, S.C., et al., *Cell-intrinsic lysosomal lipolysis is essential for alternative activation of macrophages.* Nat Immunol, 2014. **15**(9): p. 846-55.

49. Jablonski, K.A., et al., *Novel Markers to Delineate Murine M1 and M2 Macrophages.* PLoS One, 2015. **10**(12): p. e0145342.

50. Martinez, F.O., et al., *Transcriptional profiling of the human monocyte-to-macrophage differentiation and polarization: new molecules and patterns of gene expression.* J Immunol, 2006. **177**(10): p. 7303-11.

51. Piccolo, V., et al., *Opposing macrophage polarization programs show extensive epigenomic and transcriptional cross-talk.* Nat Immunol, 2017. **18**(5): p. 530-540.

52. Xue, J., et al., *Transcriptome-based network analysis reveals a spectrum model of human macrophage activation.* Immunity, 2014. **40**(2): p. 274-88.

53. Mathur, S.N., E. Albright, and F.J. Field, *12-Hydroxyeicosatetraenoic acid is metabolized by beta-oxidation in mouse peritoneal macrophages. Identification of products and proposed pathway.* J Biol Chem, 1990. **265**(34): p. 21048-55.

54. Ellis, J.M., et al., *Adipose acyl-CoA synthetase-1 directs fatty acids toward beta-oxidation and is required for cold thermogenesis.* Cell Metab, 2010. **12**(1): p. 53-64.

55. Ellis, J.M., et al., *Mouse cardiac acyl coenzyme a synthetase 1 deficiency impairs Fatty Acid oxidation and induces cardiac hypertrophy.* Mol Cell Biol, 2011. **31**(6): p. 1252-62.

56. Grevengoed, T.J., et al., *Loss of long-chain acyl-CoA synthetase isoform 1 impairs cardiac autophagy and mitochondrial structure through mechanistic target of rapamycin complex 1 activation.* FASEB J, 2015. **29**(11): p. 4641-53.

57. Grevengoed, T.J., et al., *Acyl-CoA synthetase 1 deficiency alters cardiolipin species and impairs mitochondrial function.* J Lipid Res, 2015. **56**(8): p. 1572-82.

58. Lee, K., J. Kerner, and C.L. Hoppel, *Mitochondrial carnitine palmitoyltransferase 1a (CPT1a) is part of an outer membrane fatty acid transfer complex.* J Biol Chem, 2011. **286**(29): p. 25655-62.

59. Li, L.O., et al., *Compartmentalized acyl-CoA metabolism in skeletal muscle regulates systemic glucose homeostasis.* Diabetes, 2015. **64**(1): p. 23-35.

60. Young, P.A., et al., *Long-chain acyl-CoA synthetase 1 interacts with key proteins that activate and direct fatty acids into niche hepatic pathways.* J Biol Chem, 2018. **293**(43): p. 16724-16740.

61. Klett, E.L., et al., *Long-chain acyl-CoA synthetase isoforms differ in preferences for eicosanoid species and long-chain fatty acids.* J Lipid Res, 2017. **58**(5): p. 884-894.

62. Roelands, J., et al., *Long-Chain Acyl-CoA Synthetase 1 Role in Sepsis and Immunity: Perspectives From a Parallel Review of Public Transcriptome Datasets and of the Literature.* Frontiers in Immunology, 2019. **10**(2410).

63. Janssen, U., et al., *Human mitochondrial 3,2-trans-enoyl-CoA isomerase (DCI): gene structure and localization to chromosome 16p13.3.* Genomics, 1994. **23**(1): p. 223-8.

64. Rasmussen, A.L., et al., *Systems virology identifies a mitochondrial fatty acid oxidation enzyme, dodecenoyl coenzyme A delta isomerase, required for hepatitis C virus replication and likely pathogenesis.* J Virol, 2011. **85**(22): p. 11646-54.

65. Nomura, M., et al., *Fatty acid oxidation in macrophage polarization.* Nature Immunology, 2016. **17**(3): p. 216-217.

66. Wanders, R.J.A., H.R. Waterham, and S. Ferdinandusse, *Metabolic Interplay between Peroxisomes and Other Subcellular Organelles Including Mitochondria and the Endoplasmic Reticulum.* Frontiers in Cell and Developmental Biology, 2016. **3**(83).

67. Batista-Gonzalez, A., et al., *New Insights on the Role of Lipid Metabolism in the Metabolic Reprogramming of Macrophages.* Frontiers in Immunology, 2020. **10**(2993).

68. Gordon, J.A., P.H. Figard, and A.A. Spector, *Identification of the major metabolite of 12-HETE produced by renal tubular epithelial cells.* J Lipid Res, 1989. **30**(5): p. 731-8.

69. Gordon, J.A., P.H. Figard, and A.A. Spector, *Hydroxyeicosatetraenoic acid metabolism in cultured human skin fibroblasts. Evidence for peroxisomal beta-oxidation.* J Clin Invest, 1990. **85**(4): p. 1173-81.

70. Cyrus, T., et al., *Disruption of the 12/15-lipoxygenase gene diminishes atherosclerosis in apo E-deficient mice.* J Clin Invest, 1999. **103**(11): p. 1597-604.

71. Kitamura, T., et al., *Retrovirus-mediated gene transfer and expression cloning: powerful tools in functional genomics.* Exp Hematol, 2003. **31**(11): p. 1007-14.

72. Ipseiz, N., et al., *Effective In Vivo Gene Modification in Mouse Tissue-Resident Peritoneal Macrophages by Intraperitoneal Delivery of Lentiviral Vectors.* Mol Ther Methods Clin Dev, 2020. **16**: p. 21-31.

73. Ostermann, A.I., I. Willenberg, and N.H. Schebb, *Comparison of sample preparation methods for the quantitative analysis of eicosanoids and other oxylipins in plasma by means of LC-MS/MS.* Anal Bioanal Chem, 2015. **407**(5): p. 1403-14.

74. Kolde, R., *Pheatmap: pretty heatmaps*. 2012.

75. Davies, L.C., et al., *Peritoneal tissue-resident macrophages are metabolically poised to engage microbes using tissue-niche fuels.* Nature Communications, 2017. **8**(1): p. 2074.

76. Redmann, M., et al., *Methods for assessing mitochondrial quality control mechanisms and cellular consequences in cell culture.* Redox Biol, 2018. **17**: p. 59-69.

77. Ritchie, M.E., et al., *limma powers differential expression analyses for RNA-sequencing and microarray studies.* Nucleic Acids Research, 2015. **43**(7): p. e47-e47.

78. Carvalho, B.S. and R.A. Irizarry, *A framework for oligonucleotide microarray preprocessing.* Bioinformatics, 2010. **26**(19): p. 2363-2367.

79. Du, P., W.A. Kibbe, and S.M. Lin, *lumi: a pipeline for processing Illumina microarray.* Bioinformatics, 2008. **24**(13): p. 1547-8.

80. Kreuger, F. https://www.bioinformatics.babraham.ac.uk/projects/trim_galore/. 2019.

81. Andrews, S. https://www.bioinformatics.babraham.ac.uk/projects/fastqc/. 2019.

82. Dobin, A., et al., *STAR: ultrafast universal RNA-seq aligner.* Bioinformatics, 2012. **29**(1): p. 15-21.

83. Liao, Y., G.K. Smyth, and W. Shi, *featureCounts: an efficient general purpose program for assigning sequence reads to genomic features.* Bioinformatics, 2013. **30**(7): p. 923-930.

84. Love, M.I., W. Huber, and S. Anders, *Moderated estimation of fold change and dispersion for RNA-seq data with DESeq2.* Genome Biology, 2014. **15**(12): p. 550.

Figure 1

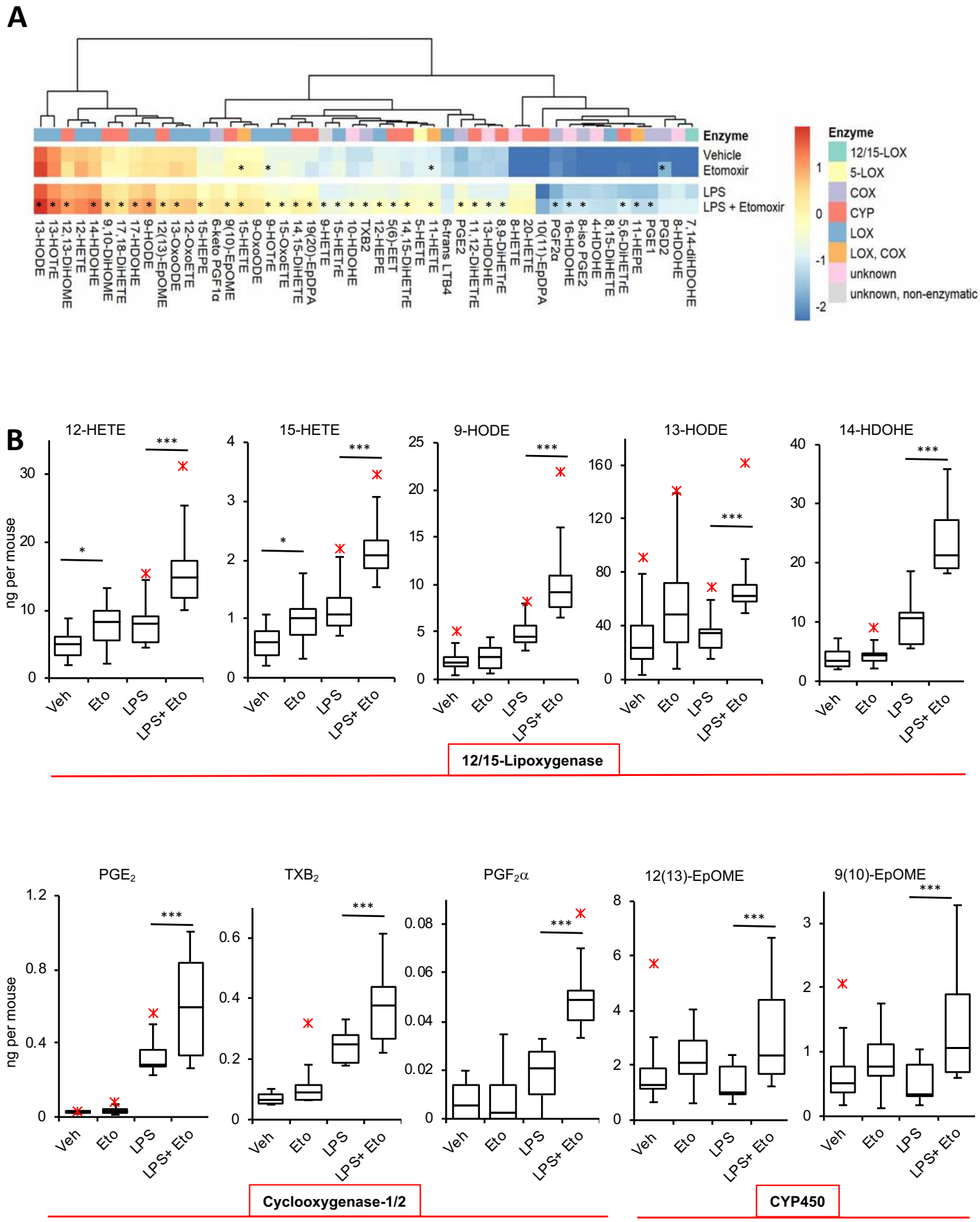
A
Enzyme
Vehicle
Etomoxir
LPS
LPS + Etomoxir
13-HODE
13-HOTrE
12,13-DiHOME
12-HETE
14-HDOHE
9,10-DiHOME
17,18-DiHETE
17-HDOHE
9-HODE
12(13)-EpOME
13-OxoODE
12-OxoETE
15-HEPE
6-keto PGF1α
9(10)-EpOME
15-HETE
9-OxoODE
9-HOTrE
15-OxoETE
14,15-DiHETE
19(20)-EpDPA
9-HETE
15-HETrE
10-HDOHE
TXB2
12-HEPE
5(6)-EET
14,15-DiHETrE
5-HETE
11-HETE
6-trans LTB4
PGE2
11,12-DiHETrE
13-HDOHE
8,9-DiHETrE
8-HETE
20-HETE
10(11)-EpDPA
PGF2α
16-HDOHE
8-iso PGE2
4-HDOHE
8,15-DiHETE
5,6-DiHETrE
11-HEPE
PGE1
PGD2
8-HDOHE
7,14-diHDOHE
Enzyme
12/15-LOX
5-LOX
COX
CYP
LOX
LOX, COX
unknown
unknown, non-enzymatic
B
12-HETE
15-HETE
9-HODE
13-HODE
14-HDOHE
ng per mouse
Veh
Eto
LPS
LPS+ Eto
12/15-Lipoxygenase
PGE2
TXB2
PGF2α
12(13)-EpOME
9(10)-EpOME
Cyclooxygenase-1/2
CYP450

Figure 2

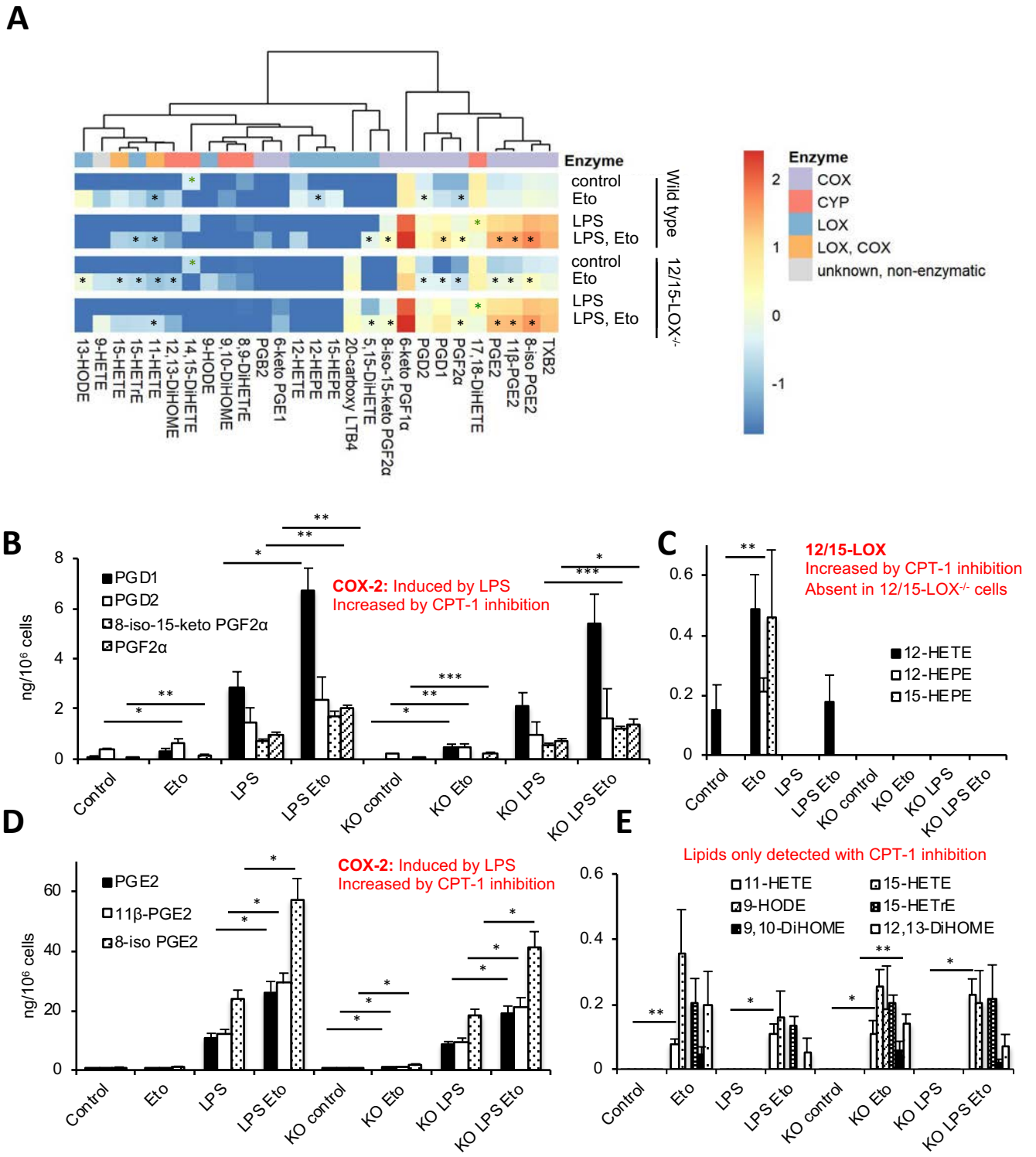
A
Enzyme
control
Eto
LPS
LPS, Eto
Wild type
12/15-LOX-/-
13-HODE
9-HETE
15-HETE
15-HETrE
11-HETE
12,13-DiHOME
14,15-DiHETE
9-HODE
9,10-DiHOME
8,9-DiHETrE
PGB2
6-keto PGE1
12-HETE
12-HEPE
15-HEPE
20-carboxy LTB4
5,15-DiHETE
8-iso-15-keto PGF2α
6-keto PGF1α
PGD2
PGD1
PGF2α
17,18-DiHETE
PGE2
11β-PGE2
8-iso PGE2
TXB2
Enzyme
COX
CYP
LOX
LOX, COX
unknown, non-enzymatic
B
ng/10⁶ cells
PGD1
PGD2
8-iso-15-keto PGF2α
PGF2α
COX-2: Induced by LPS
Increased by CPT-1 inhibition
Control
Eto
LPS
LPS Eto
KO control
KO Eto
KO LPS
KO LPS Eto
C
12/15-LOX
Increased by CPT-1 inhibition
Absent in 12/15-LOX-/- cells
12-HETE
12-HEPE
15-HEPE
D
ng/10⁶ cells
PGE2
11β-PGE2
8-iso PGE2
COX-2: Induced by LPS
Increased by CPT-1 inhibition
E
Lipids only detected with CPT-1 inhibition
11-HETE
9-HODE
9,10-DiHOME
15-HETE
15-HETrE
12,13-DiHOME

Figure 3

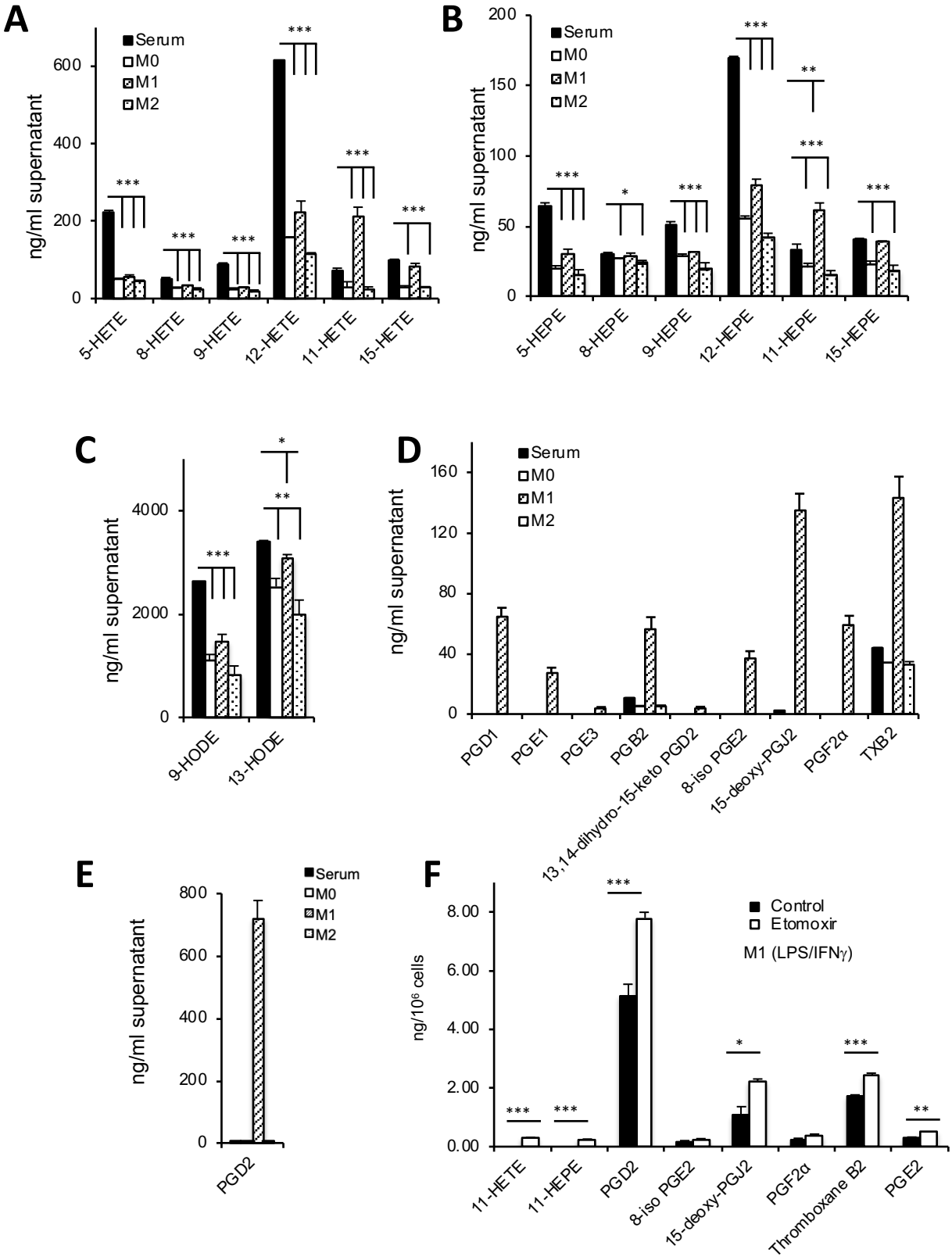
A
Serum
M0
M1
M2
ng/ml supernatant
0
200
400
600
***
5-HETE
8-HETE
9-HETE
12-HETE
11-HETE
15-HETE
B
200
150
100
50
0
**
*
5-HEPE
8-HEPE
9-HEPE
12-HEPE
11-HEPE
15-HEPE
C
4000
2000
9-HODE
13-HODE
D
160
120
80
40
PGD1
PGE1
PGE3
PGB2
13,14-dihydro-15-keto PGD2
8-iso PGE2
15-deoxy-PGJ2
PGF2α
TXB2
E
800
PGD2
F
Control
Etomoxir
M1 (LPS/IFNγ)
ng/10⁶ cells
8.00
6.00
4.00
2.00
0.00
11-HETE
11-HEPE
PGD2
8-iso PGE2
15-deoxy-PGJ2
PGF2α
Thromboxane B2
PGE2

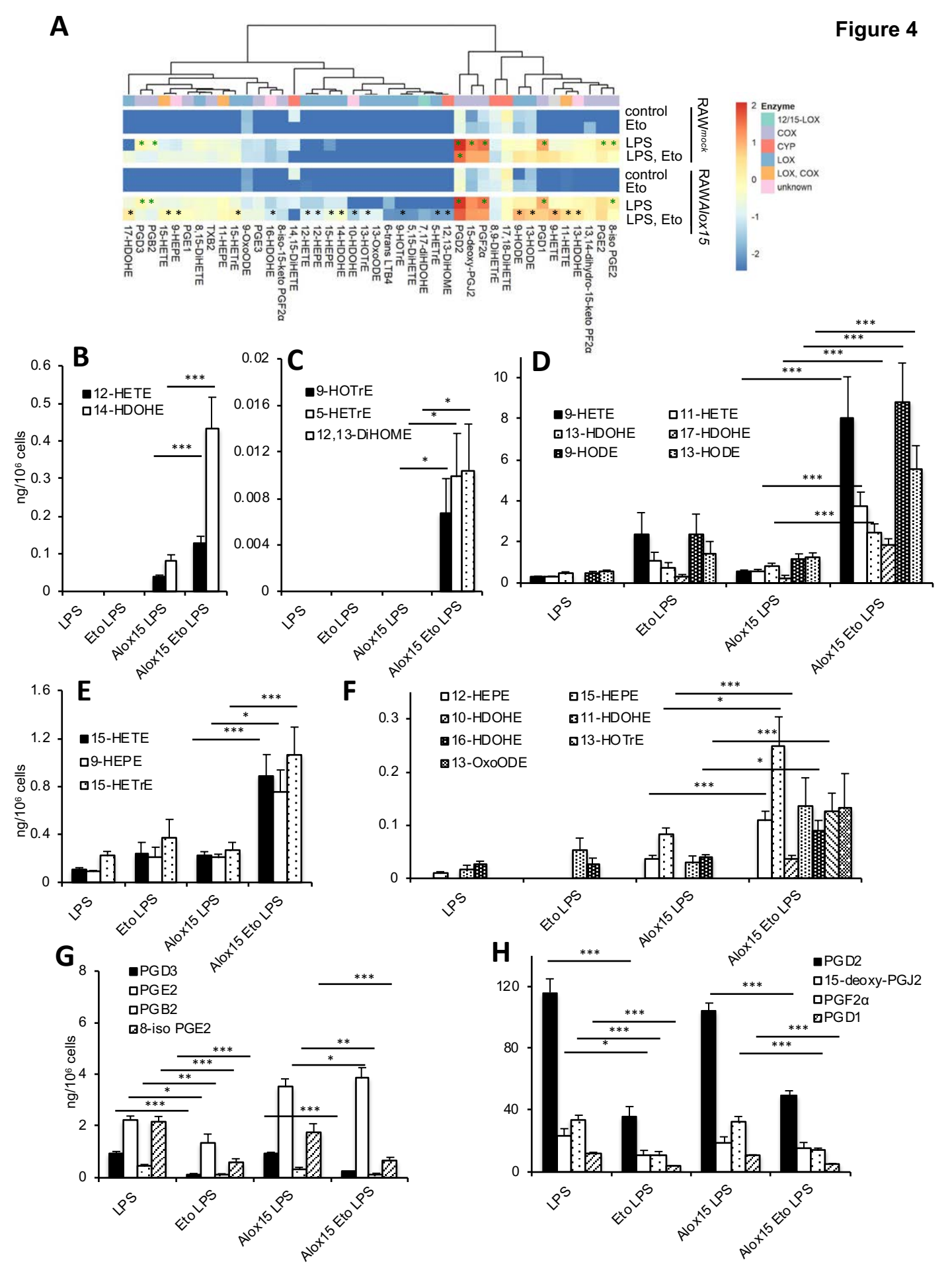
Figure 4
A
control
Eto
LPS
LPS, Eto
RAWmock
RAWAlox15
Enzyme
12/15-LOX
COX
CYP
LOX
LOX, COX
unknown
17-HDOHE
PGD3
PGB2
15-HETE
9-HEPE
PGE1
8,15-DiHETE
TXB2
11-HEPE
15-HETrE
9-OxoODE
PGE3
16-HDOHE
8-iso-15-keto PGF2α
14,15-DiHETE
12-HETE
12-HEPE
15-HEPE
14-HDOHE
10-HDOHE
13-HOTrE
13-OxoODE
6-trans LTB4
9-HOTrE
5,15-DiHETE
7,17-diHDOHE
5-HETrE
PGD2
12,13-DiHOME
15-deoxy-PGJ2
PGF2α
8,9-DiHETrE
17,18-DiHETE
9-HODE
13-HODE
PGD1
9-HETE
11-HETE
13-HDOHE
13,14-dihydro-15-keto PF2α
PGE2
8-iso PGE2
B
12-HETE
14-HDOHE
ng/10^6 cells
C
9-HOTrE
5-HETrE
12,13-DiHOME
D
9-HETE
11-HETE
13-HDOHE
17-HDOHE
9-HODE
13-HODE
E
15-HETE
9-HEPE
15-HETrE
F
12-HEPE
15-HEPE
10-HDOHE
11-HDOHE
16-HDOHE
13-HOTrE
13-OxoODE
G
PGD3
PGE2
PGB2
8-iso PGE2
H
PGD2
15-deoxy-PGJ2
PGF2α
PGD1
LPS
Eto LPS
Alox15 LPS
Alox15 Eto LPS

Figure 5

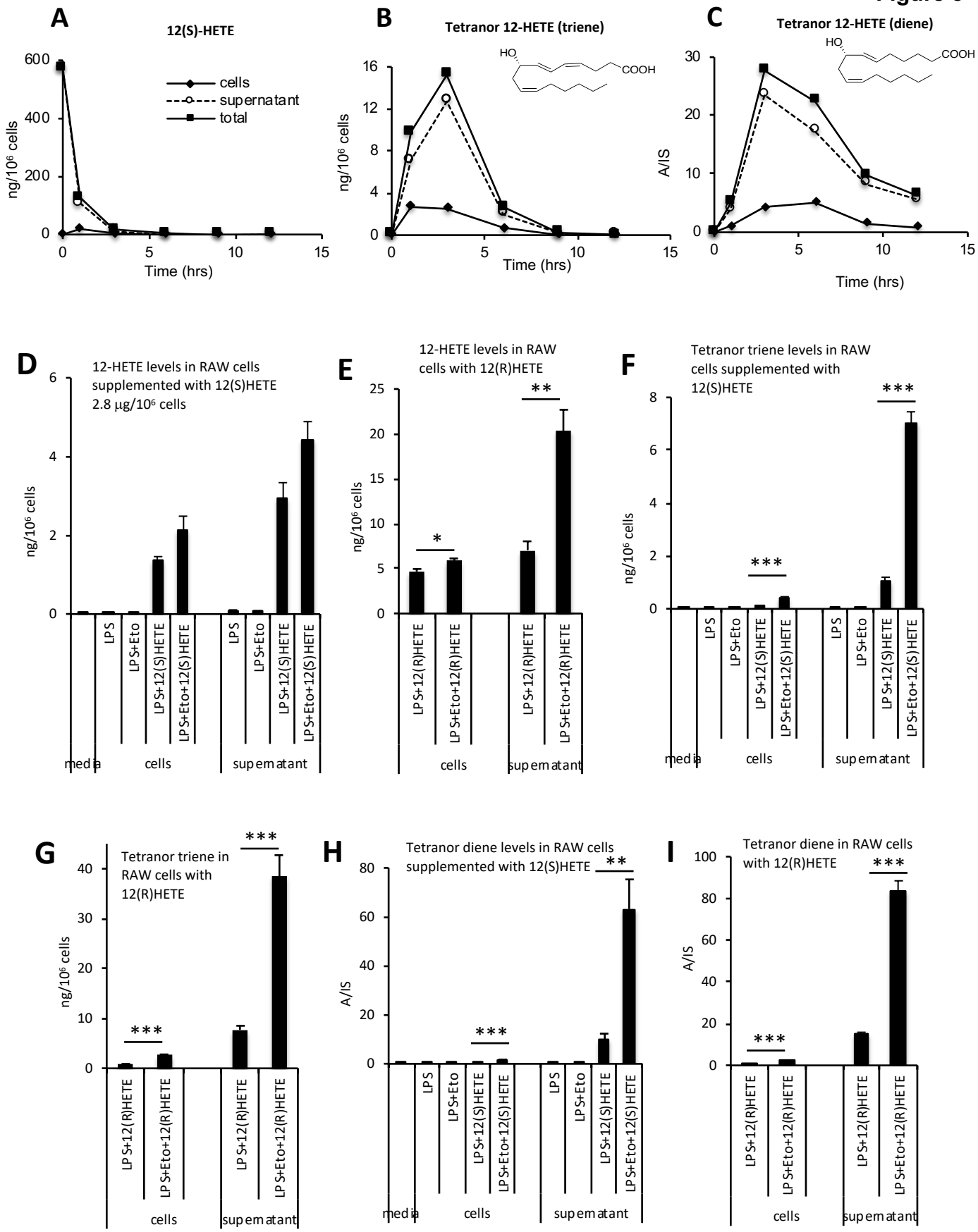
A
12(S)-HETE
cells
supernatant
total
ng/10⁶ cells
Time (hrs)
B
Tetranor 12-HETE (triene)
HO
COOH
ng/10⁶ cells
Time (hrs)
C
Tetranor 12-HETE (diene)
HO
COOH
A/IS
Time (hrs)
D
12-HETE levels in RAW cells supplemented with 12(S)HETE 2.8 µg/10⁶ cells
ng/10⁶ cells
LPS
LPS+Eto
LPS+12(S)HETE
LPS+Eto+12(S)HETE
media
cells
supernatant
E
12-HETE levels in RAW cells with 12(R)HETE
ng/10⁶ cells
LPS+12(R)HETE
LPS+Eto+12(R)HETE
cells
supernatant
F
Tetranor triene levels in RAW cells supplemented with 12(S)HETE
ng/10⁶ cells
LPS
LPS+Eto
LPS+12(S)HETE
LPS+Eto+12(S)HETE
media
cells
supernatant
G
Tetranor triene in RAW cells with 12(R)HETE
ng/10⁶ cells
LPS+12(R)HETE
LPS+Eto+12(R)HETE
cells
supernatant
H
Tetranor diene levels in RAW cells supplemented with 12(S)HETE
A/IS
LPS
LPS+Eto
LPS+12(S)HETE
LPS+Eto+12(S)HETE
media
cells
supernatant
I
Tetranor diene in RAW cells with 12(R)HETE
A/IS
LPS+12(R)HETE
LPS+Eto+12(R)HETE
cells
supernatant

Figure 6

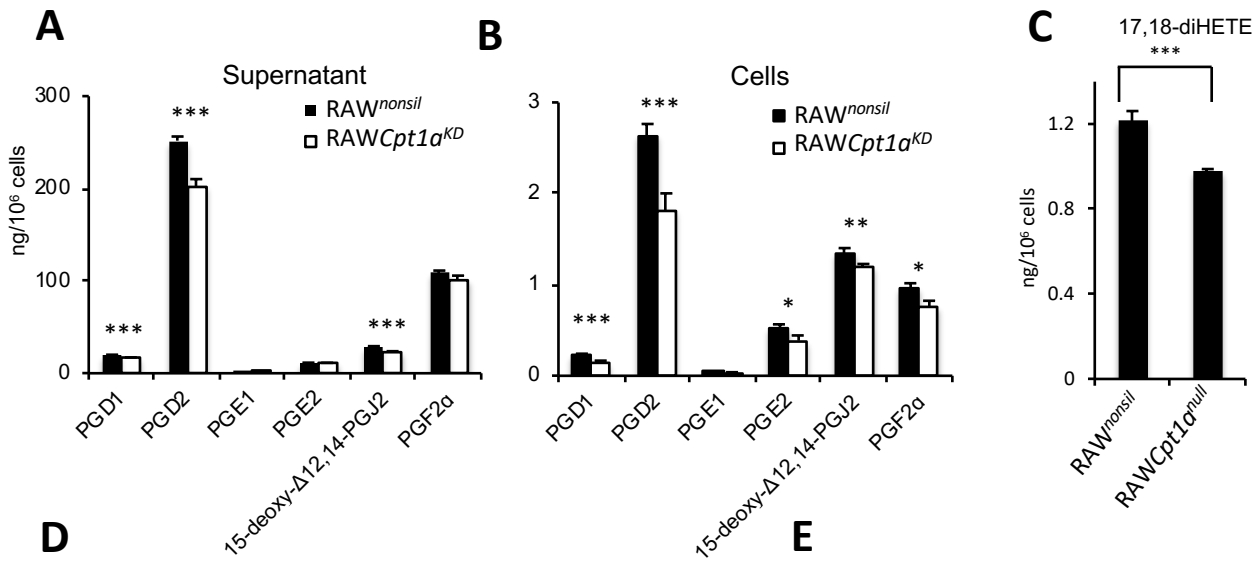

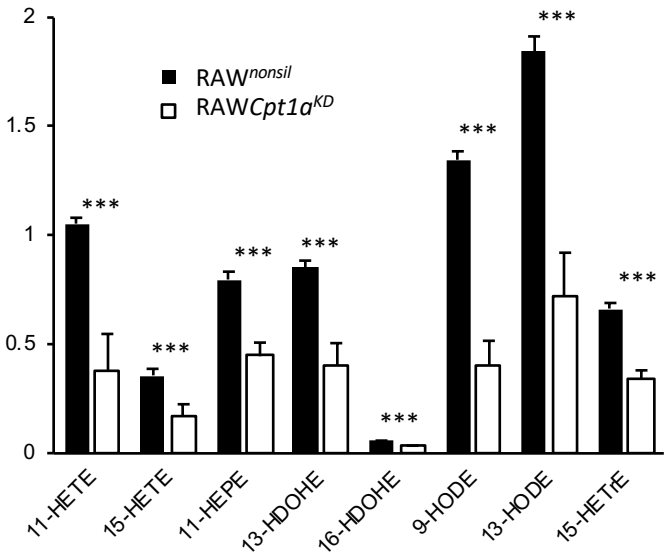

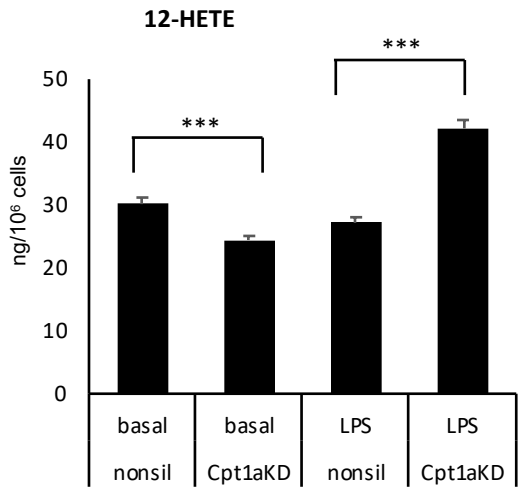

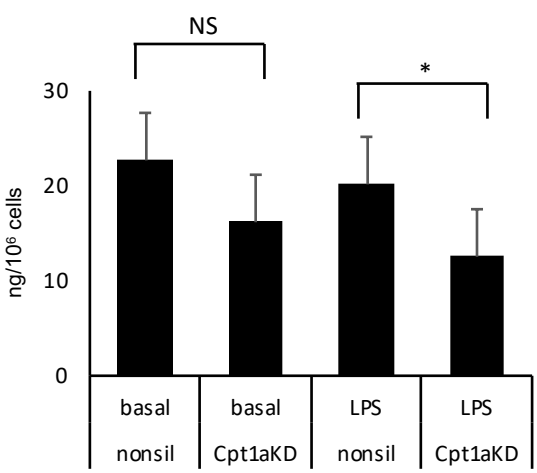

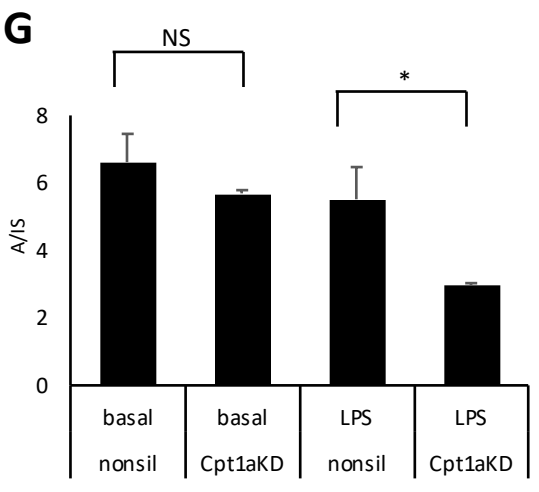

Tetranor 12-HETE (triene)

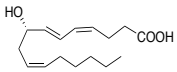

Tetranor 12-HETE (diene)

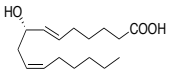

Figure 7

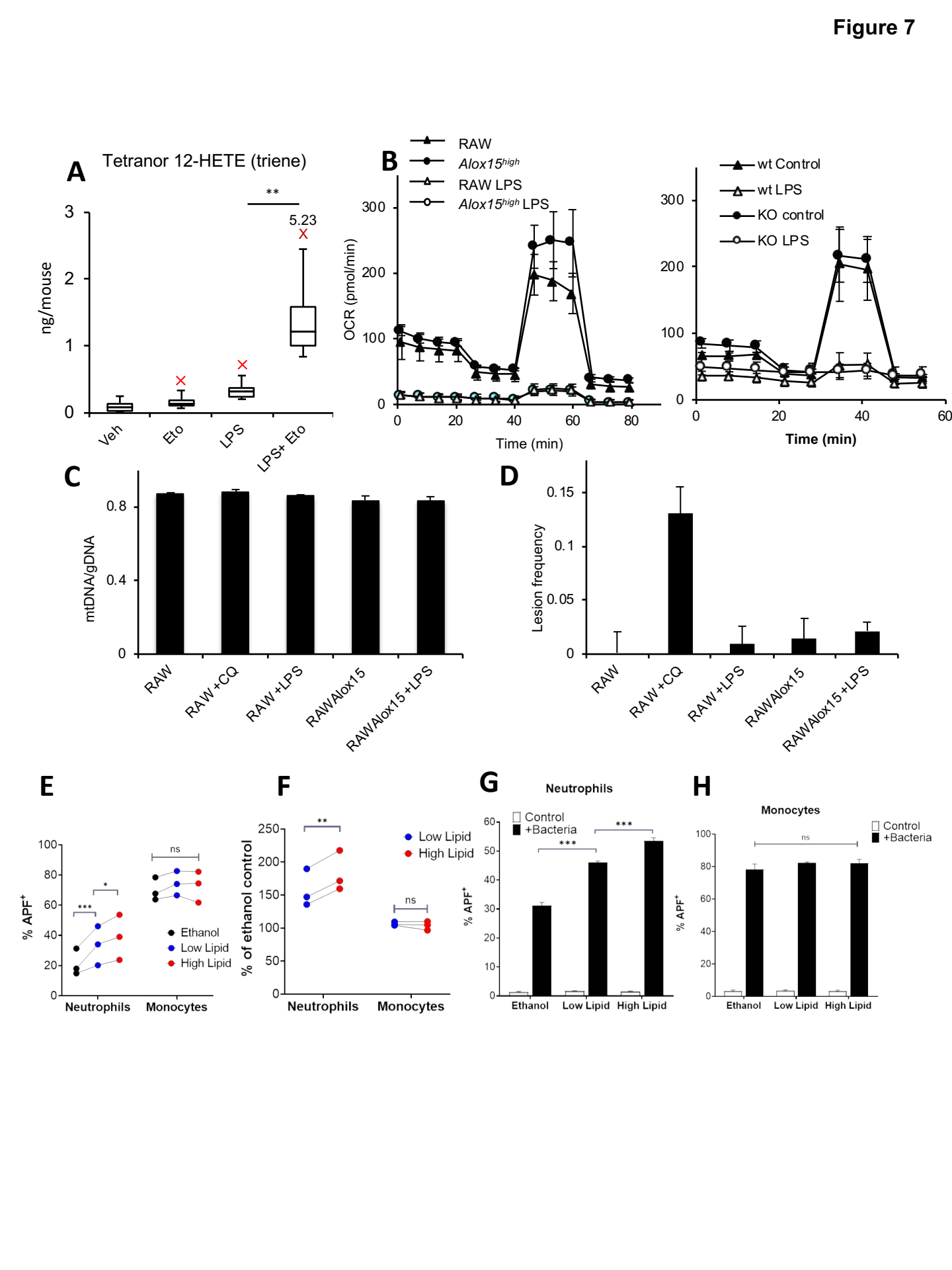
A
Tetranor 12-HETE (triene)
ng/mouse
**
5.23
Veh
Eto
LPS
LPS+ Eto
B
RAW
Alox15high
RAW LPS
Alox15high LPS
OCR (pmol/min)
Time (min)
wt Control
wt LPS
KO control
KO LPS
Time (min)
C
mtDNA/gDNA
RAW
RAW +CQ
RAW +LPS
RAWAlox15
RAWAlox15+LPS
D
Lesion frequency
RAW
RAW +CQ
RAW +LPS
RAWAlox15
RAWAlox15+LPS
E
% APF+
***
*
ns
Ethanol
Low Lipid
High Lipid
Neutrophils
Monocytes
F
% of ethanol control
**
ns
Low Lipid
High Lipid
Neutrophils
Monocytes
G
Neutrophils
Control
+Bacteria
***
***
% APF+
Ethanol
Low Lipid
High Lipid
H
Monocytes
Control
+Bacteria
ns
% APF+
Ethanol
Low Lipid
High Lipid

Figure 8

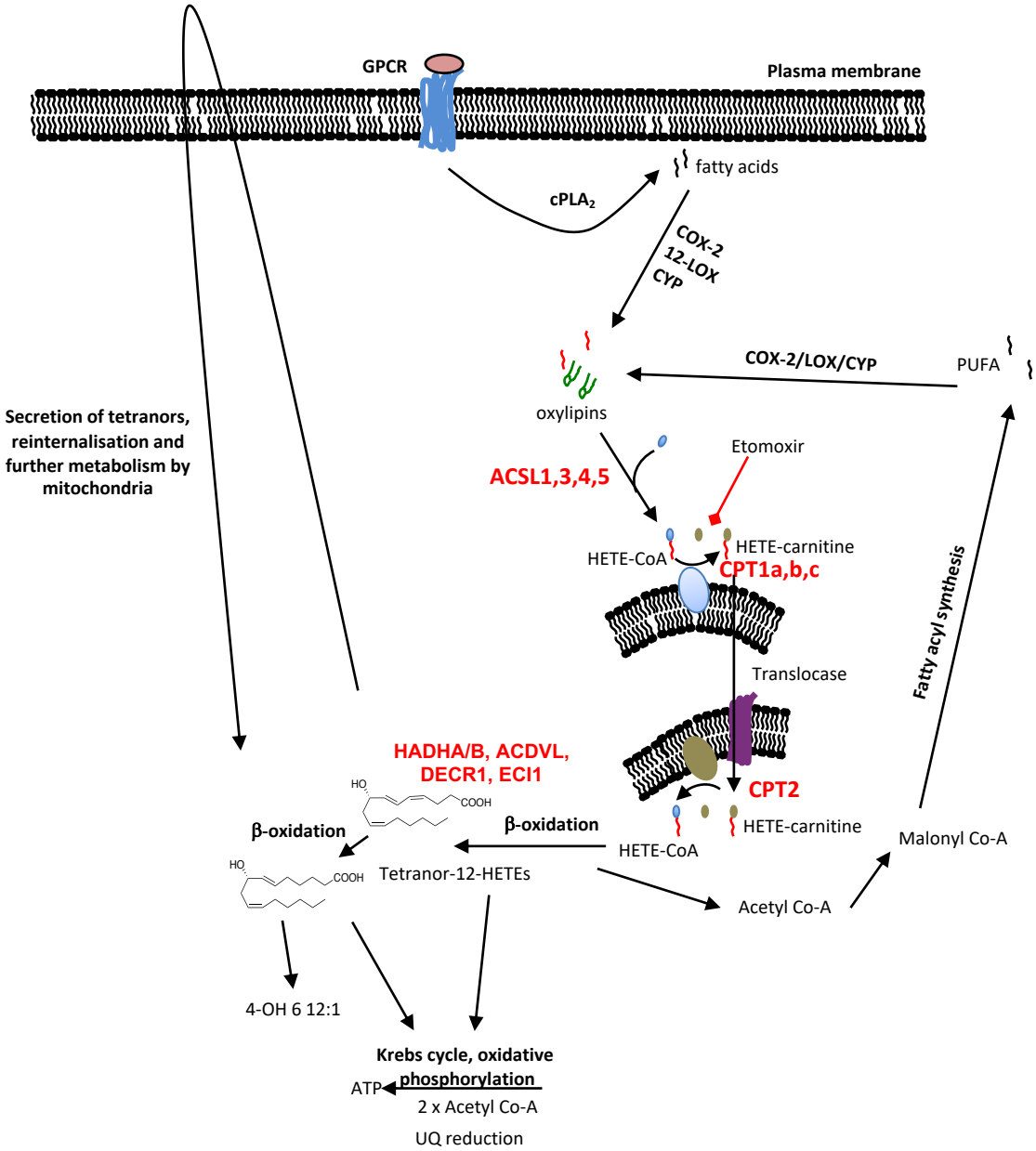
GPCR
Plasma membrane
fatty acids
cPLA2
COX-2
12-LOX
CYP
COX-2/LOX/CYP
PUFA
oxylipins
Secretion of tetranors, reinternalisation and further metabolism by mitochondria
Etomoxir
ACSL1,3,4,5
HETE-CoA
HETE-carnitine
CPT1a,b,c
Translocase
Fatty acyl synthesis
HADHA/B, ACDVL, DECR1, ECI1
CPT2
HETE-carnitine
HETE-CoA
Malonyl Co-A
β-oxidation
β-oxidation
Tetranor-12-HETEs
Acetyl Co-A
4-OH 6 12:1
Krebs cycle, oxidative phosphorylation
ATP
2 x Acetyl Co-A
UQ reduction

Figure 9

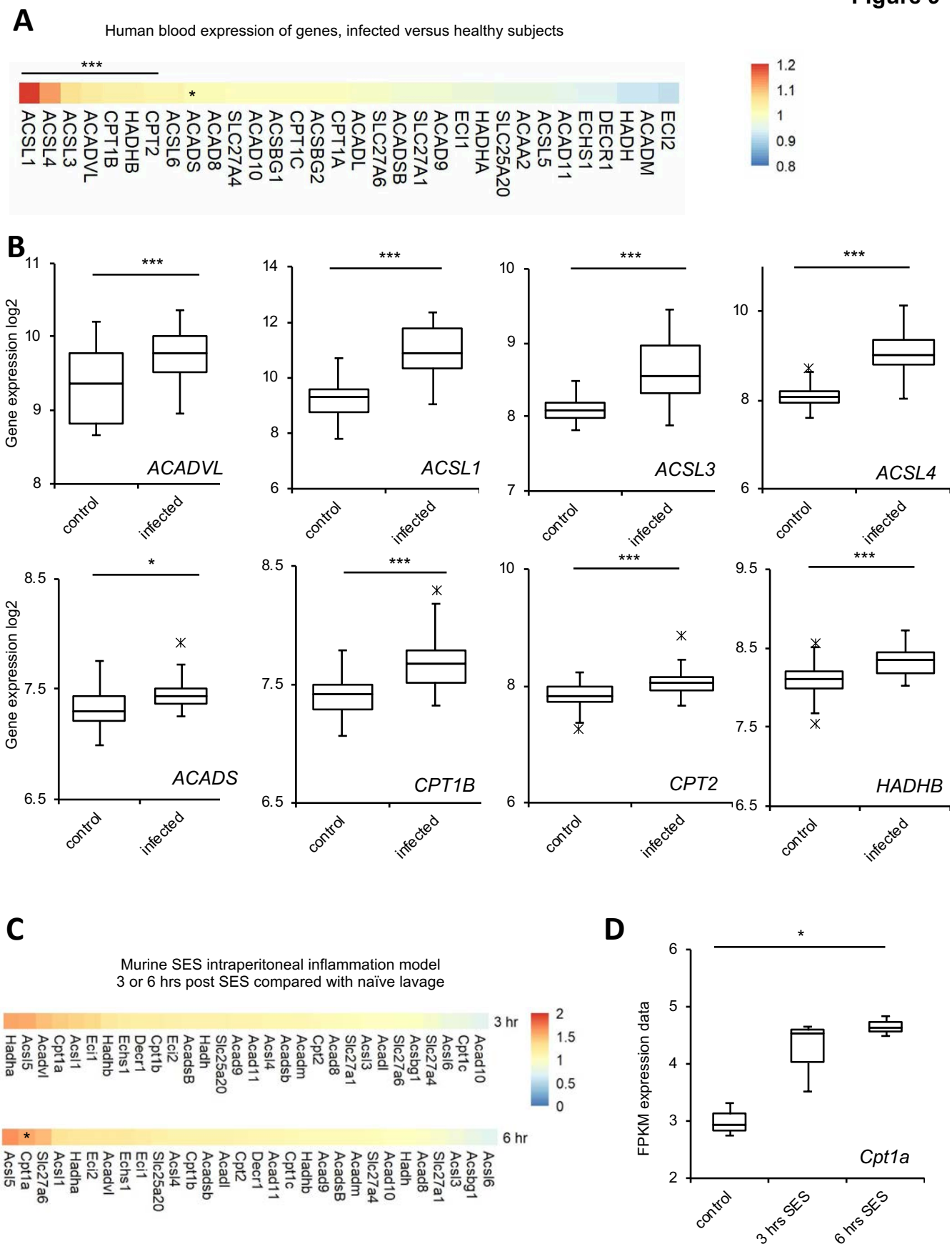
A
Human blood expression of genes, infected versus healthy subjects
***
*
ACSL1
ACSL4
ACSL3
ACADVL
CPT1B
HADHB
CPT2
ACSL6
ACADS
ACAD8
SLC27A4
ACAD10
ACSBG1
CPT1C
ACSBG2
CPT1A
ACADL
SLC27A6
ACADSB
SLC27A1
ACAD9
ECI1
HADHA
SLC25A20
ACAA2
ACSL5
ACAD11
ECHS1
DECR1
HADH
ACADM
ECI2
1.2
1.1
1
0.9
0.8
B
Gene expression log2
ACADVL
ACSL1
ACSL3
ACSL4
ACADS
CPT1B
CPT2
HADHB
control
infected
C
Murine SES intraperitoneal inflammation model
3 or 6 hrs post SES compared with naïve lavage
3 hr
6 hr
Hadha
Acsl5
Acadvl
Cpt1a
Acsl1
Eci1
Hadhb
Echs1
Decr1
Cpt1b
Eci2
AcadsB
Hadh
Slc25a20
Acad9
Acad11
Acsl4
Acadsb
Acadm
Cpt2
Acad8
Slc27a1
Acsl3
Acadl
Slc27a6
Acsbg1
Slc27a4
Acsl6
Cpt1c
Acad10
Slc27a6
Acsl1
Hadha
Eci2
Acadvl
Echs1
Eci1
Slc25a20
Acsl4
Cpt1b
Acadsb
Acadl
Cpt2
Decr1
Acad11
Cpt1c
Hadhb
Acad9
AcadsB
Acadm
Slc27a4
Acad10
Hadh
Acad8
Slc27a1
Acsbg1
Acsl6
2
1.5
1
0.5
0
D
FPKM expression data
Cpt1a
control
3 hrs SES
6 hrs SES

Figure 10

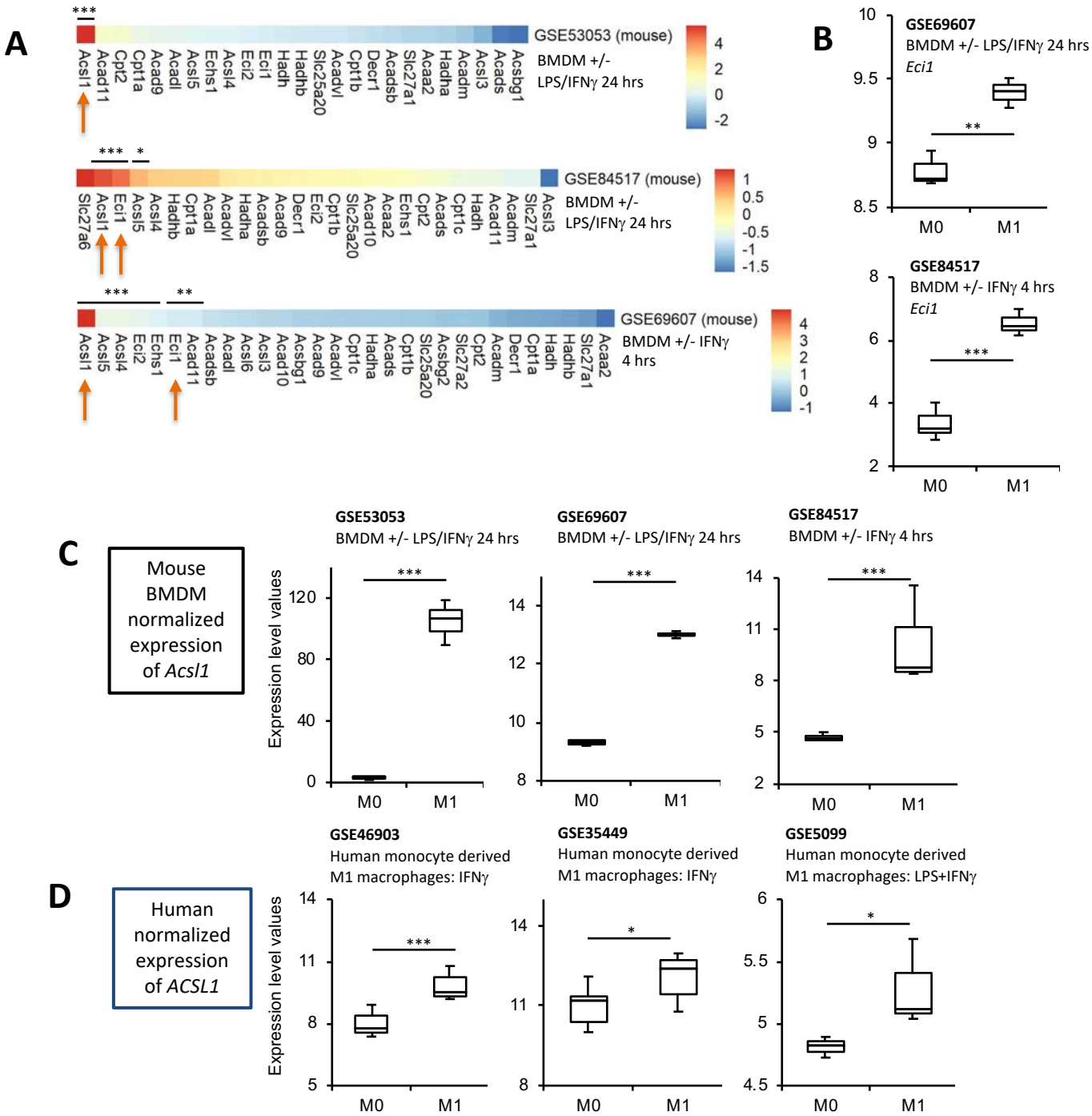
A
GSE53053 (mouse)
BMDM +/-
LPS/IFNγ 24 hrs
GSE84517 (mouse)
BMDM +/-
LPS/IFNγ 24 hrs
GSE69607 (mouse)
BMDM +/- IFNγ
4 hrs
B
GSE69607
BMDM +/- LPS/IFNγ 24 hrs
Eci1
GSE84517
BMDM +/- IFNγ 4 hrs
Eci1
M0
M1
C
Mouse
BMDM
normalized
expression
of Acsl1
GSE53053
BMDM +/- LPS/IFNγ 24 hrs
GSE69607
BMDM +/- LPS/IFNγ 24 hrs
GSE84517
BMDM +/- IFNγ 4 hrs
Expression level values
D
Human
normalized
expression
of ACSL1
GSE46903
Human monocyte derived
M1 macrophages: IFNγ
GSE35449
Human monocyte derived
M1 macrophages: IFNγ
GSE5099
Human monocyte derived
M1 macrophages: LPS+IFNγ

Scheme 1

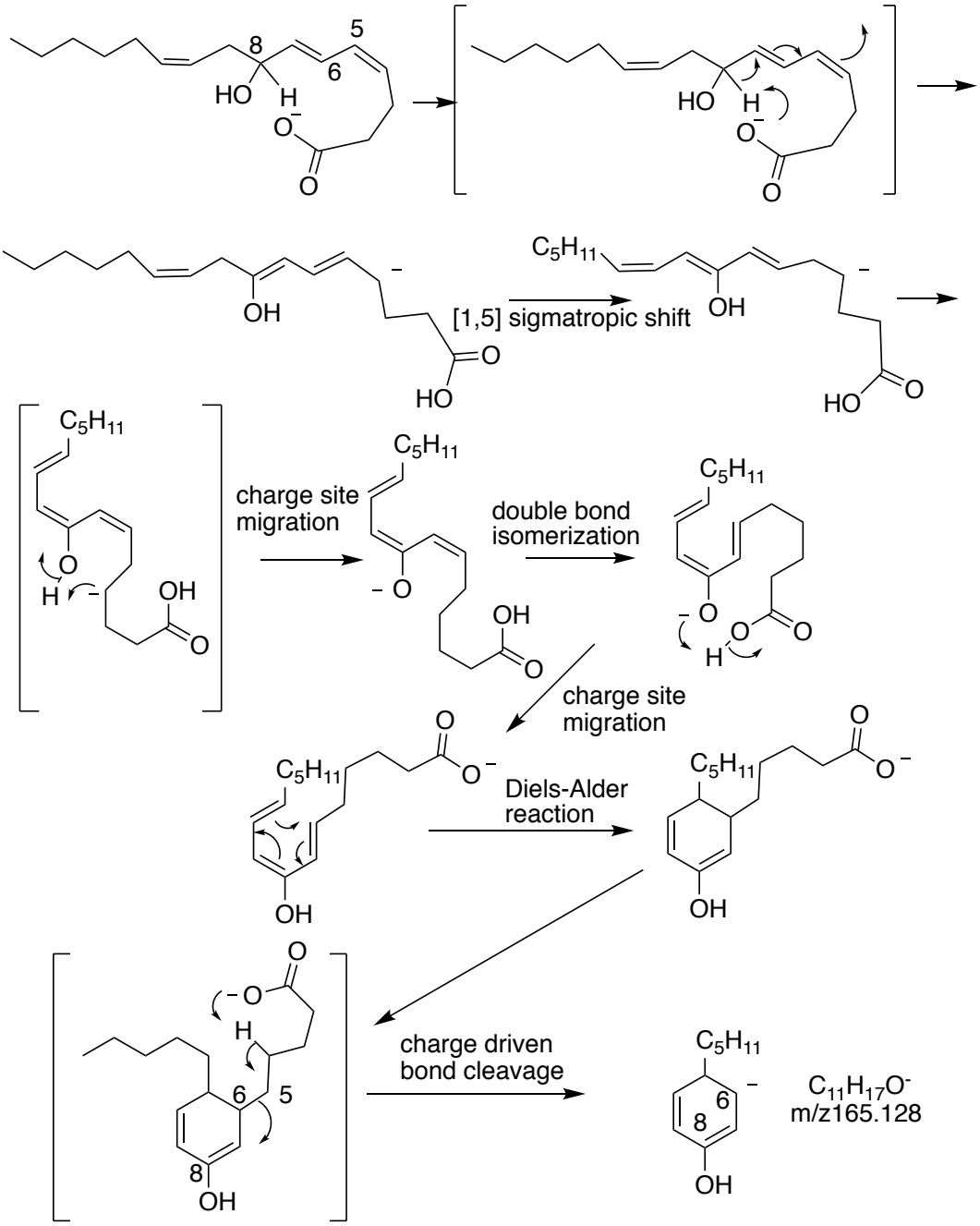

8
5
6
HO
H
O
O
HO
H
O
O
OH
O
HO
[1,5] sigmatropic shift
C5H11
OH
O
HO
C5H11
O
H
OH
O
charge site
migration
C5H11
O
OH
O
double bond
isomerization
C5H11
O
O
O
H
charge site
migration
O
C5H11
O
OH
Diels-Alder
reaction
C5H11
O
O
OH
O
O
H
6
5
8
OH
charge driven
bond cleavage
C5H11
6
8
OH
C11H17O-
m/z165.128

Scheme 2

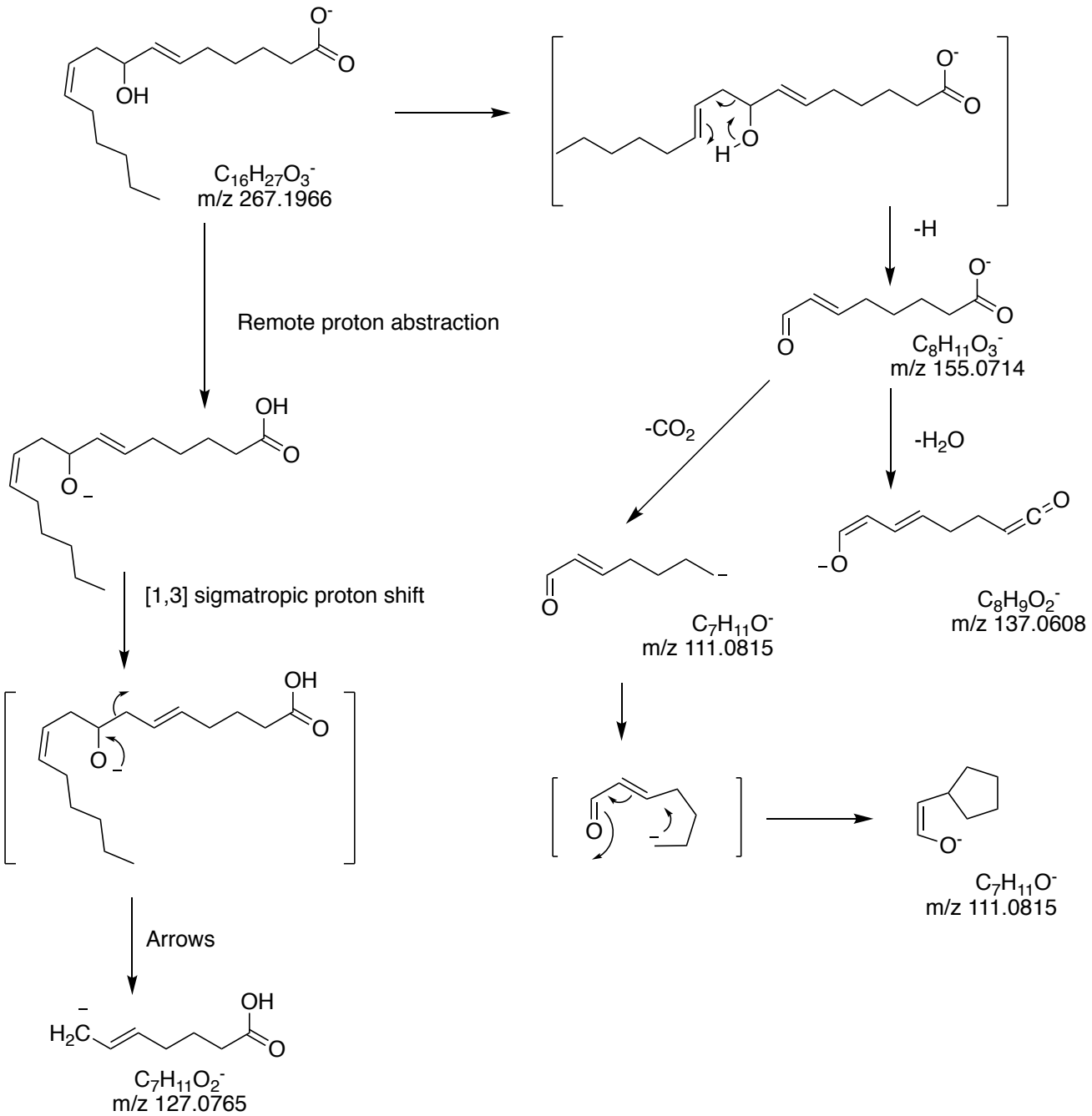
$C_{16}H_{27}O_3^-$
m/z 267.1966
Remote proton abstraction
-H
$C_8H_{11}O_3^-$
m/z 155.0714
$-CO_2$
$-H_2O$
$C_7H_{11}O^-$
m/z 111.0815
$C_8H_9O_2^-$
m/z 137.0608
$C_7H_{11}O^-$
m/z 111.0815
[1,3] sigmatropic proton shift
Arrows
$C_7H_{11}O_2^-$
m/z 127.0765

Scheme 3

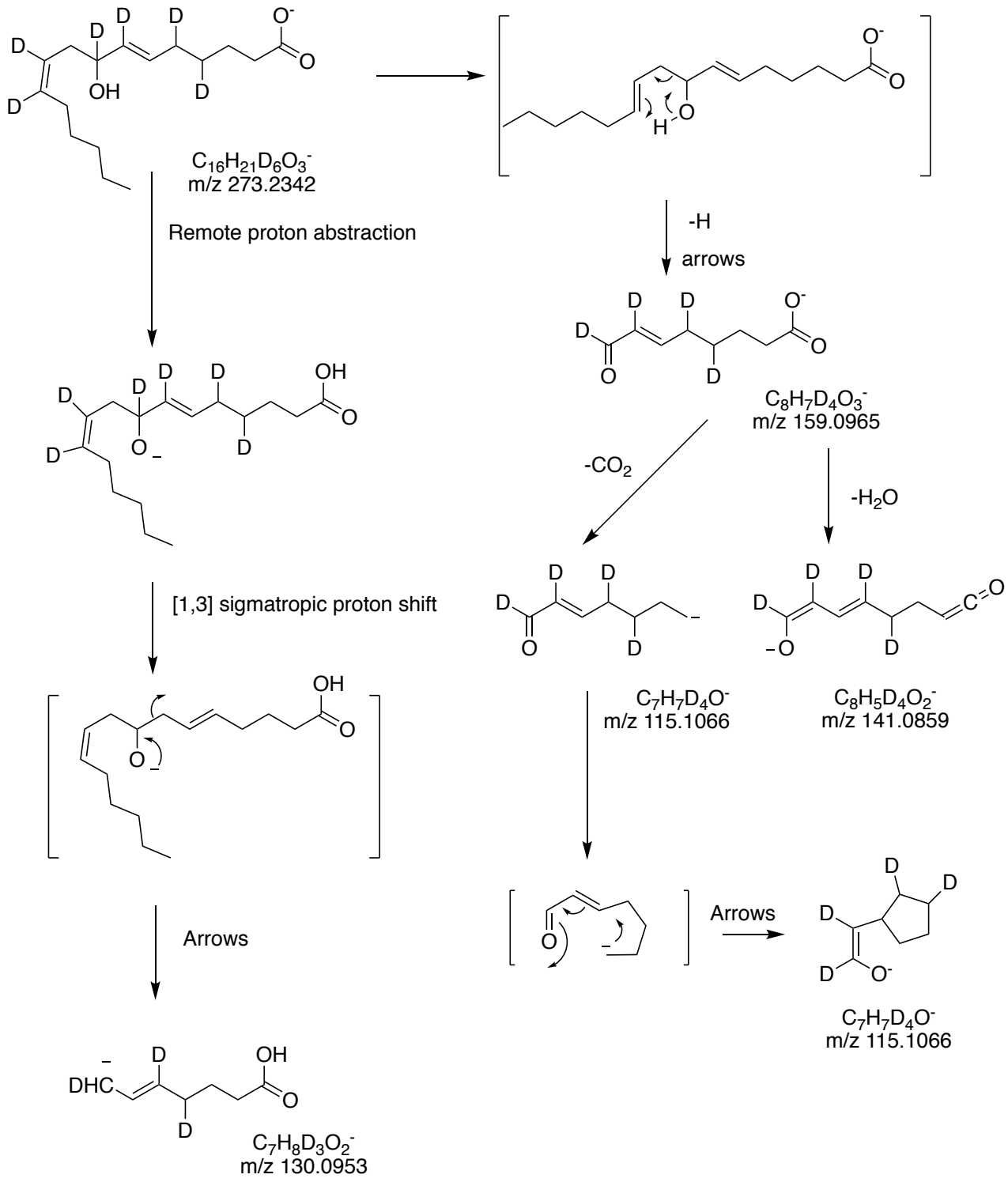
$C_{16}H_{21}D_6O_3^-$
m/z 273.2342
Remote proton abstraction
-H
arrows
$C_8H_7D_4O_3^-$
m/z 159.0965
$-CO_2$
$-H_2O$
[1,3] sigmatropic proton shift
$C_7H_7D_4O^-$
m/z 115.1066
$C_8H_5D_4O_2^-$
m/z 141.0859
Arrows
Arrows
$C_7H_7D_4O^-$
m/z 115.1066
$C_7H_8D_3O_2^-$
m/z 130.0953

Scheme 4

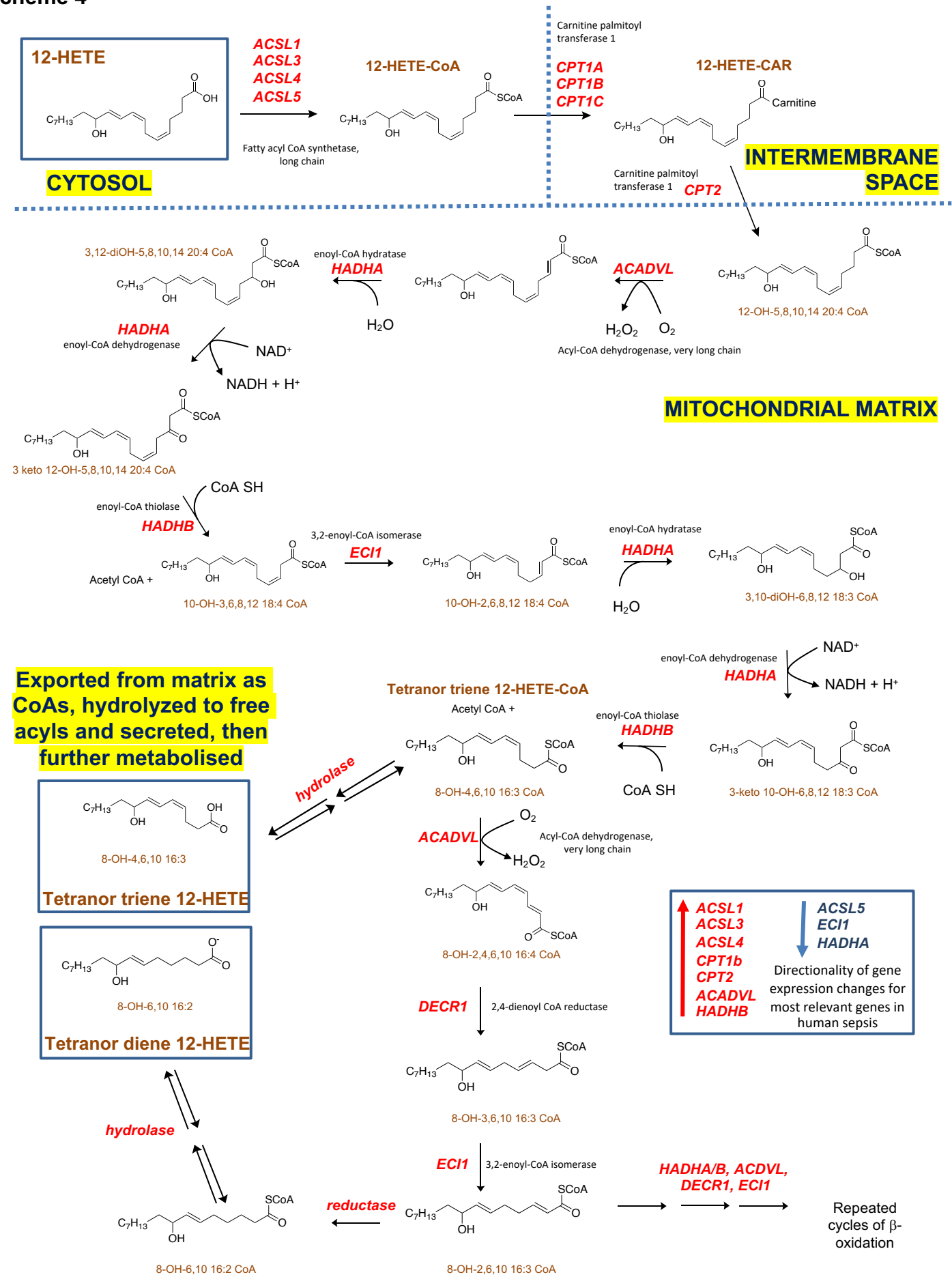
12-HETE
ACSL1
ACSL3
ACSL4
ACSL5
Fatty acyl CoA synthetase, long chain
12-HETE-CoA
Carnitine palmitoyl transferase 1
CPT1A
CPT1B
CPT1C
12-HETE-CAR
Carnitine
CYTOSOL
INTERMEMBRANE SPACE
Carnitine palmitoyl transferase 1
CPT2
3,12-diOH-5,8,10,14 20:4 CoA
enoyl-CoA hydratase
HADHA
H2O
ACADVL
H2O2
O2
Acyl-CoA dehydrogenase, very long chain
12-OH-5,8,10,14 20:4 CoA
HADHA
enoyl-CoA dehydrogenase
NAD+
NADH + H+
MITOCHONDRIAL MATRIX
3 keto 12-OH-5,8,10,14 20:4 CoA
CoA SH
enoyl-CoA thiolase
HADHB
Acetyl CoA +
10-OH-3,6,8,12 18:4 CoA
3,2-enoyl-CoA isomerase
ECI1
10-OH-2,6,8,12 18:4 CoA
enoyl-CoA hydratase
HADHA
H2O
3,10-diOH-6,8,12 18:3 CoA
enoyl-CoA dehydrogenase
HADHA
NAD+
NADH + H+
3-keto 10-OH-6,8,12 18:3 CoA
enoyl-CoA thiolase
HADHB
CoA SH
Tetranor triene 12-HETE-CoA
Acetyl CoA +
8-OH-4,6,10 16:3 CoA
Exported from matrix as CoAs, hydrolyzed to free acyls and secreted, then further metabolised
hydrolase
8-OH-4,6,10 16:3
Tetranor triene 12-HETE
ACADVL
O2
H2O2
Acyl-CoA dehydrogenase, very long chain
8-OH-2,4,6,10 16:4 CoA
8-OH-6,10 16:2
Tetranor diene 12-HETE
DECR1
2,4-dienoyl CoA reductase
8-OH-3,6,10 16:3 CoA
ACSL1
ACSL3
ACSL4
CPT1b
CPT2
ACADVL
HADHB
ACSL5
ECI1
HADHA
Directionality of gene expression changes for most relevant genes in human sepsis
hydrolase
ECI1
3,2-enoyl-CoA isomerase
HADHA/B, ACDVL, DECR1, ECI1
reductase
8-OH-6,10 16:2 CoA
8-OH-2,6,10 16:3 CoA
Repeated cycles of β-oxidation

Supplementary Figure 1

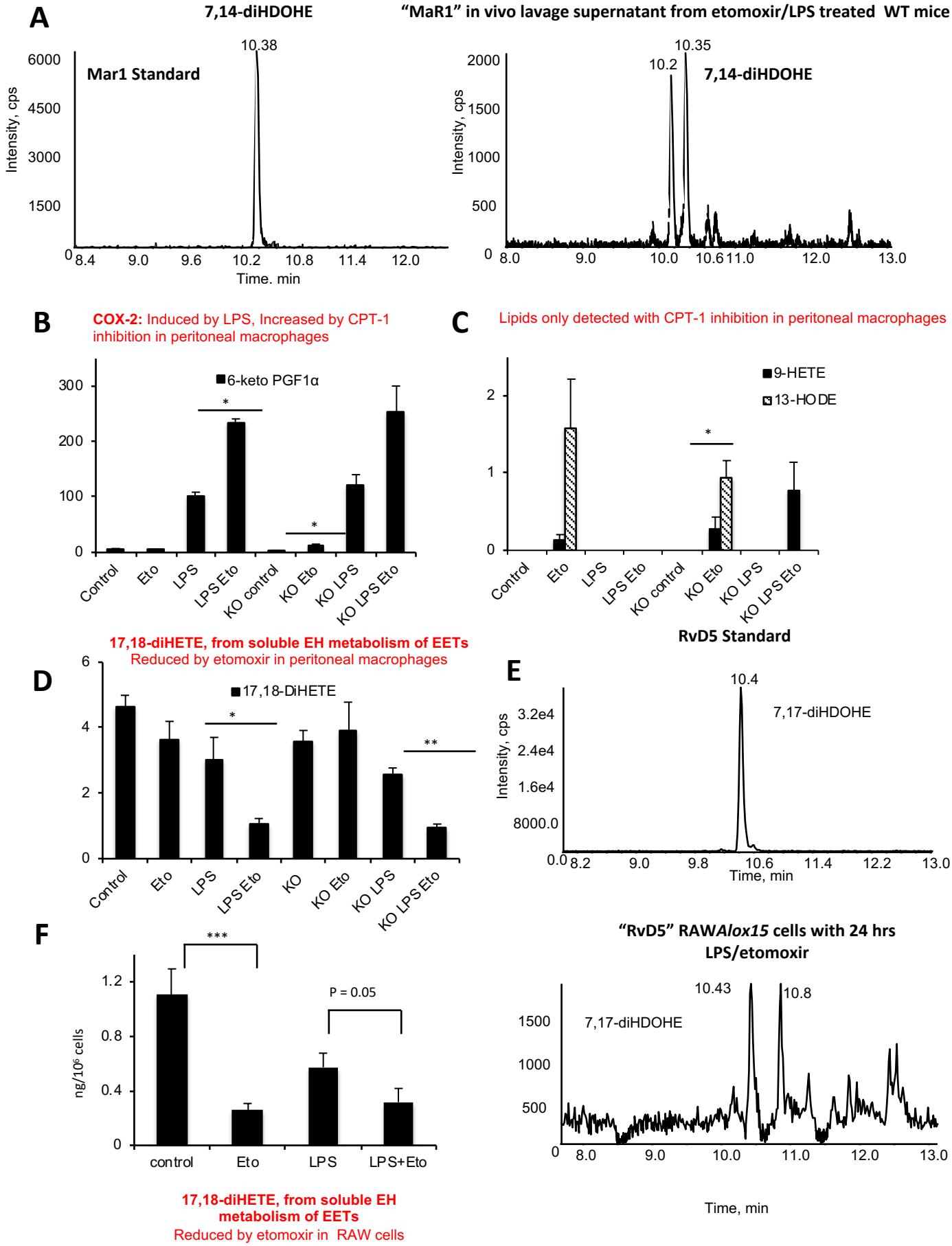

Supplementary Figure 2

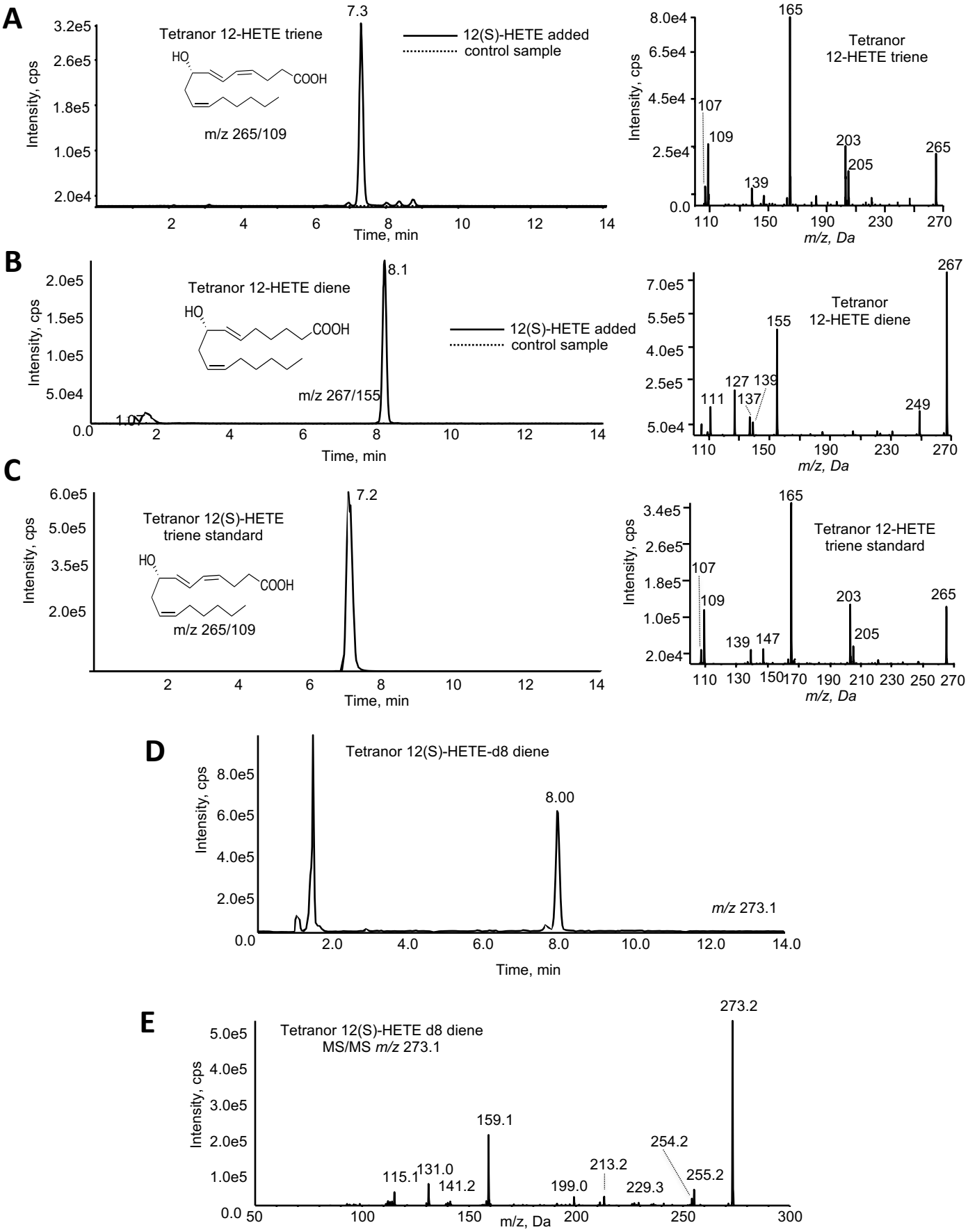

Supplementary Figure 3

A Tetranor-12(S)-HETE Extracted Ion Chromatogram 265.17-265.19amu

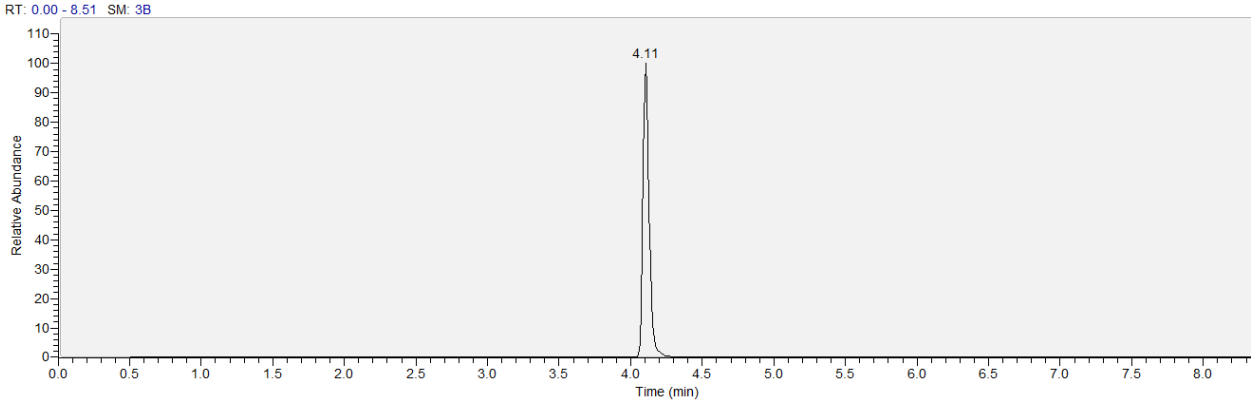

Tetranor-12(S)-HETE MS Spectrum

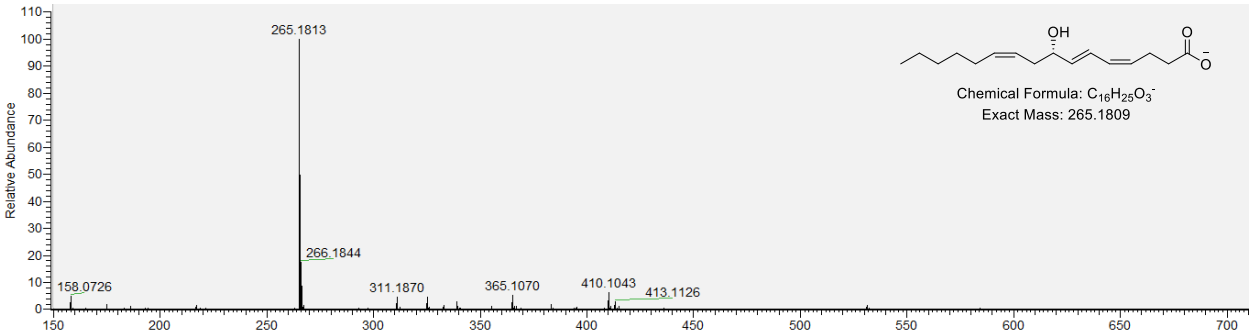

Tetranor-12(S)-HETE HCD Product Ion Spectrum

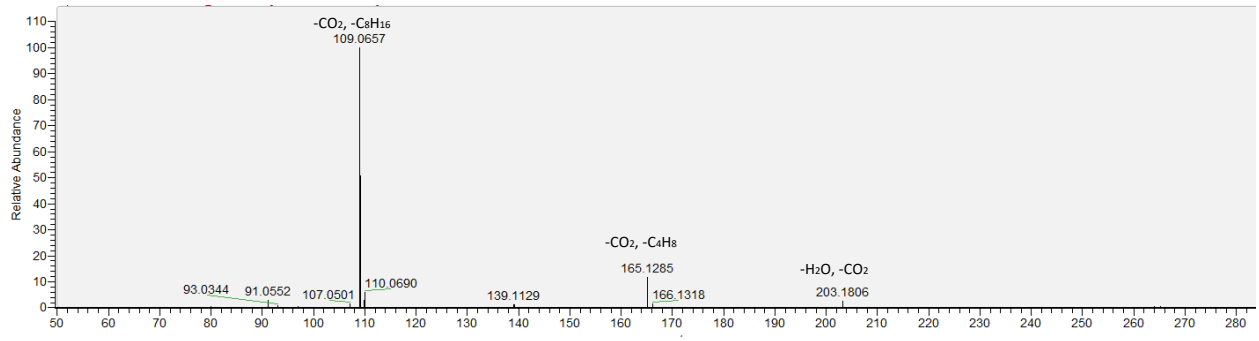

B

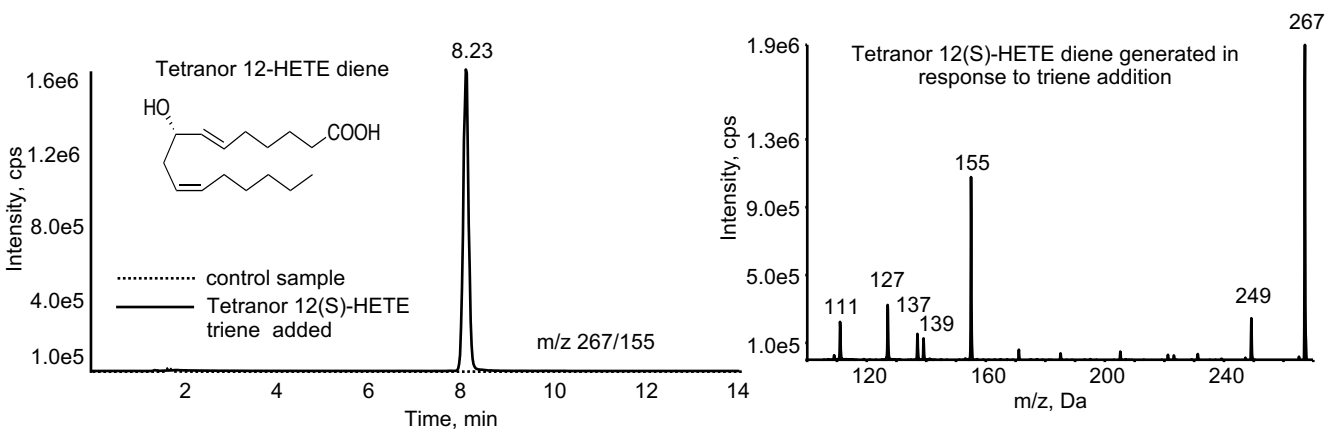

Supplementary Figure 4

A

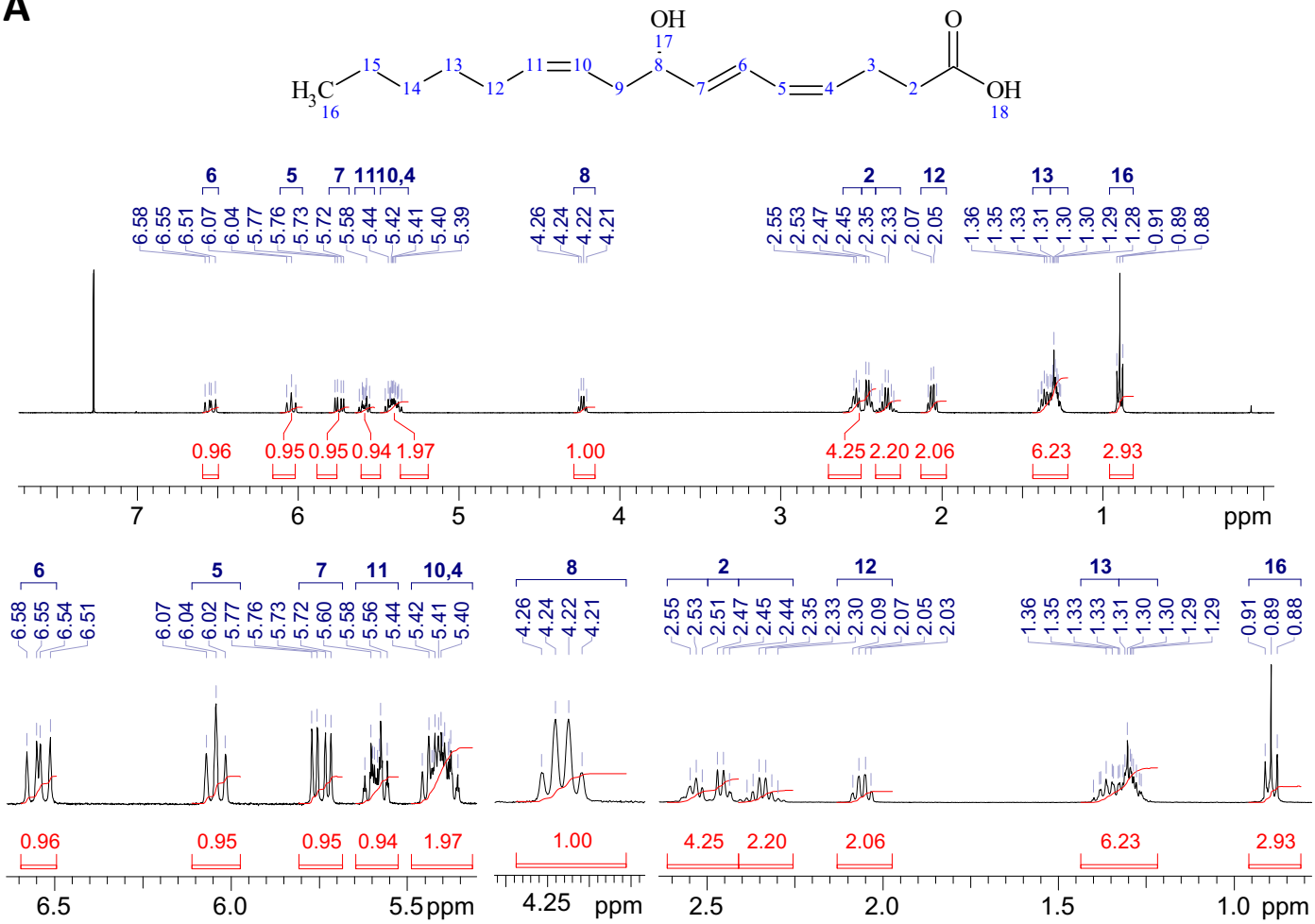

B

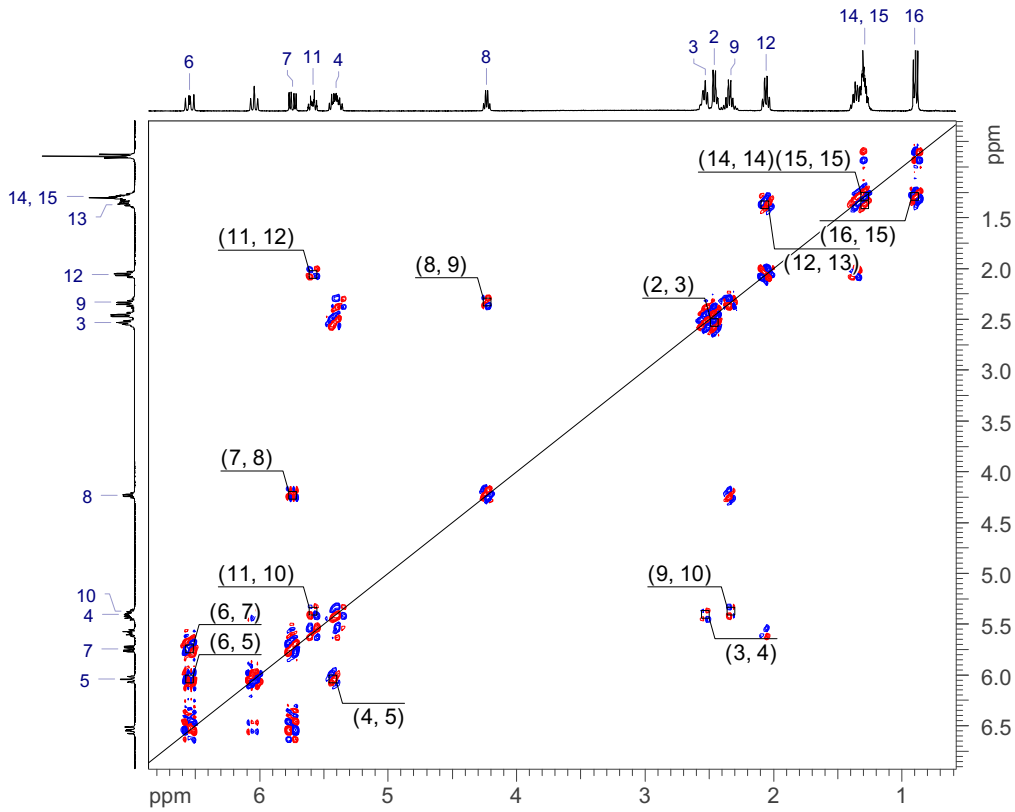

Supplementary Figure 5

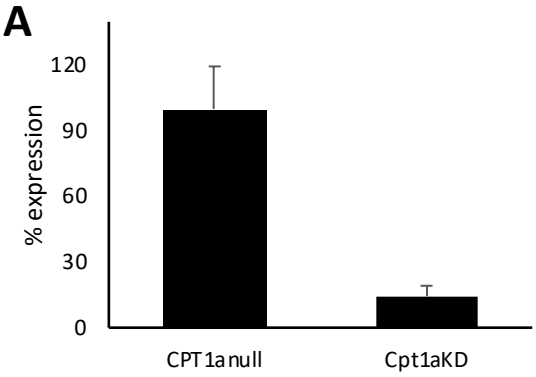

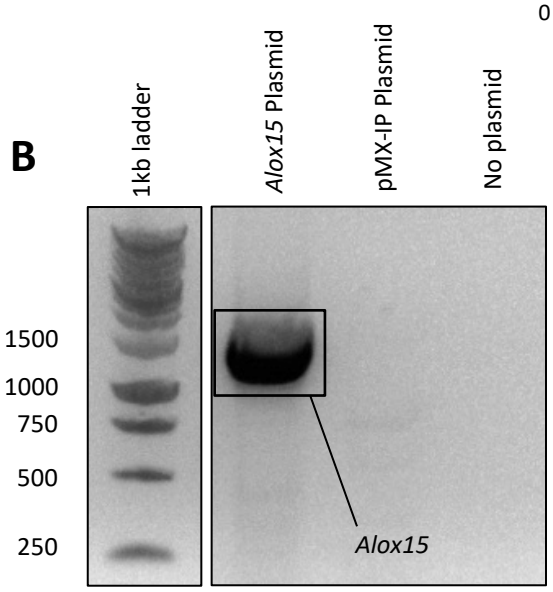

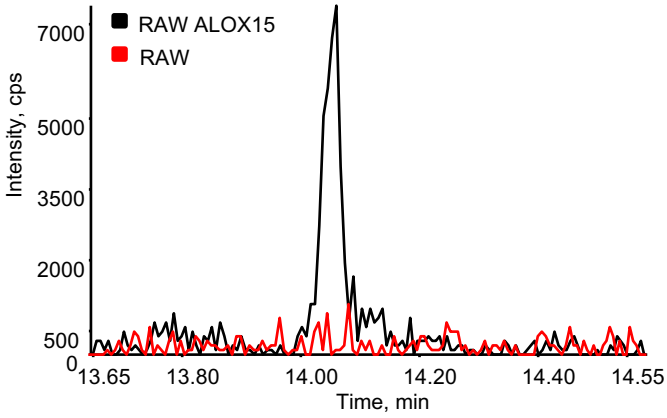

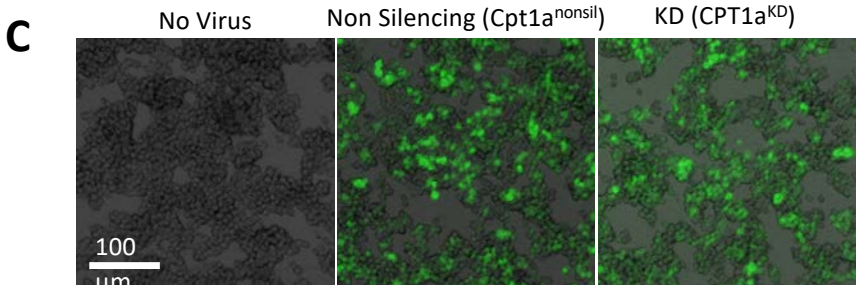

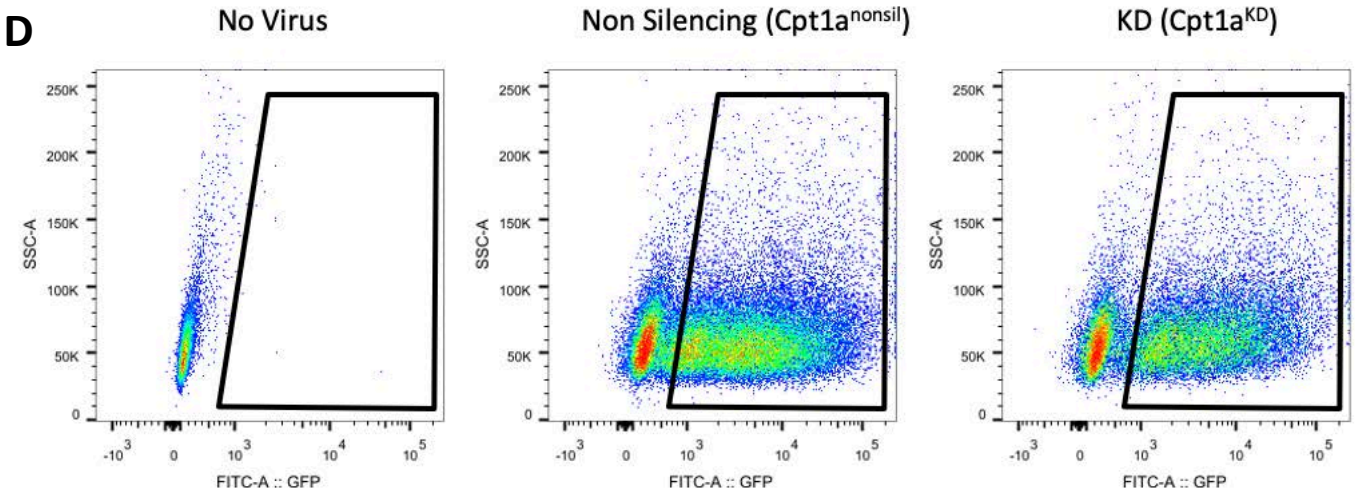

Supplementary Figure 6

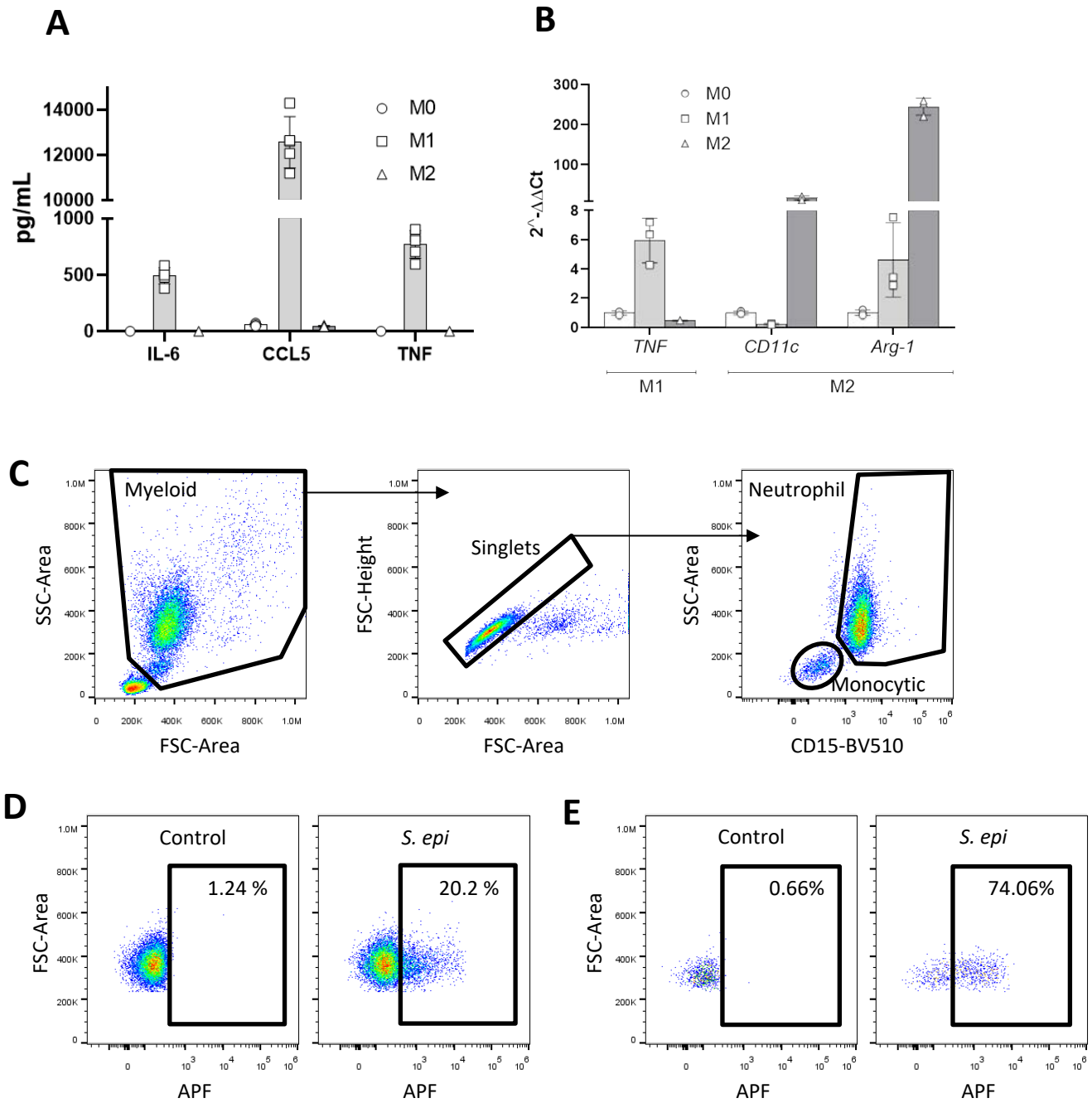

Supplementary Figure 7

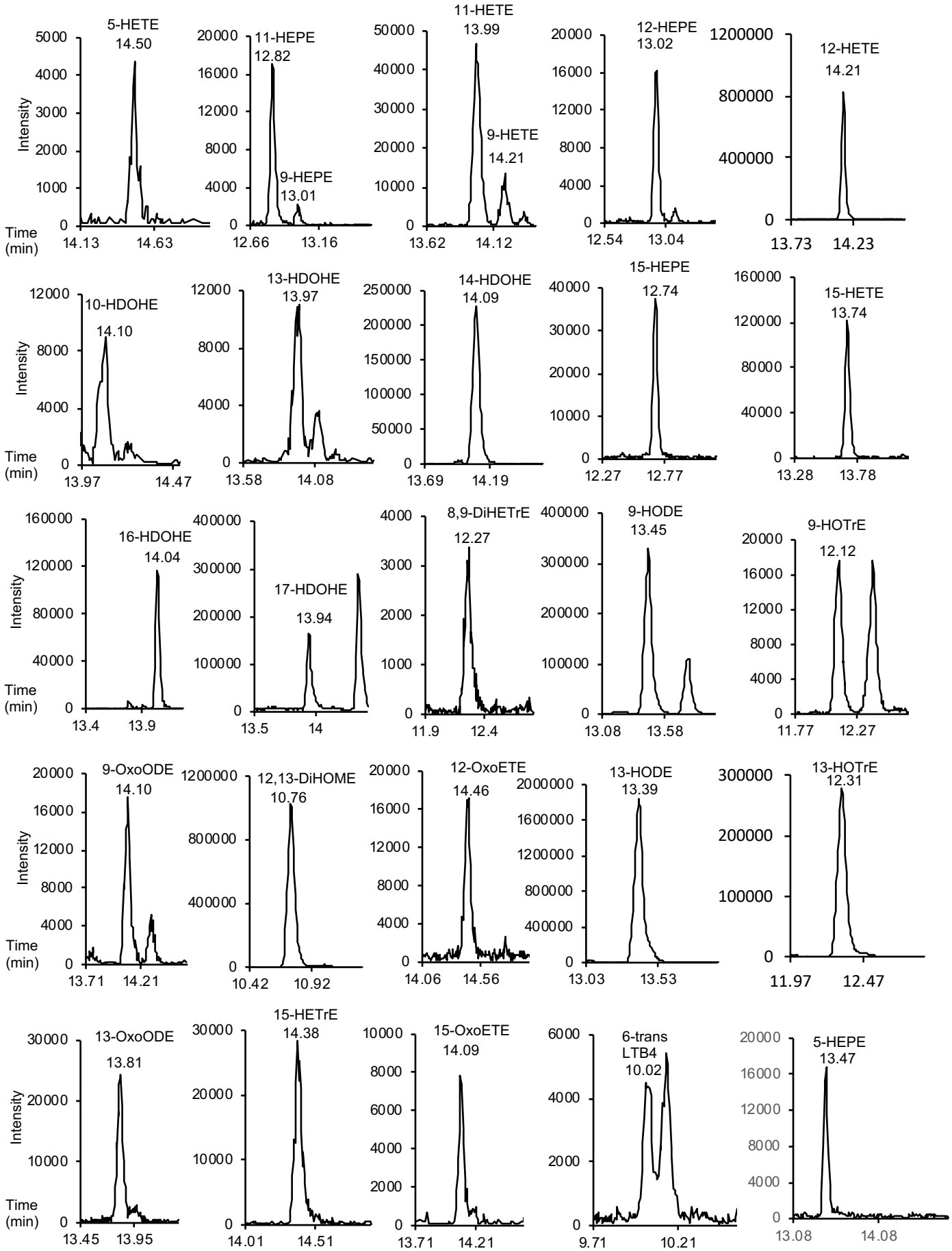

Supplementary Figure 7 (contd.)

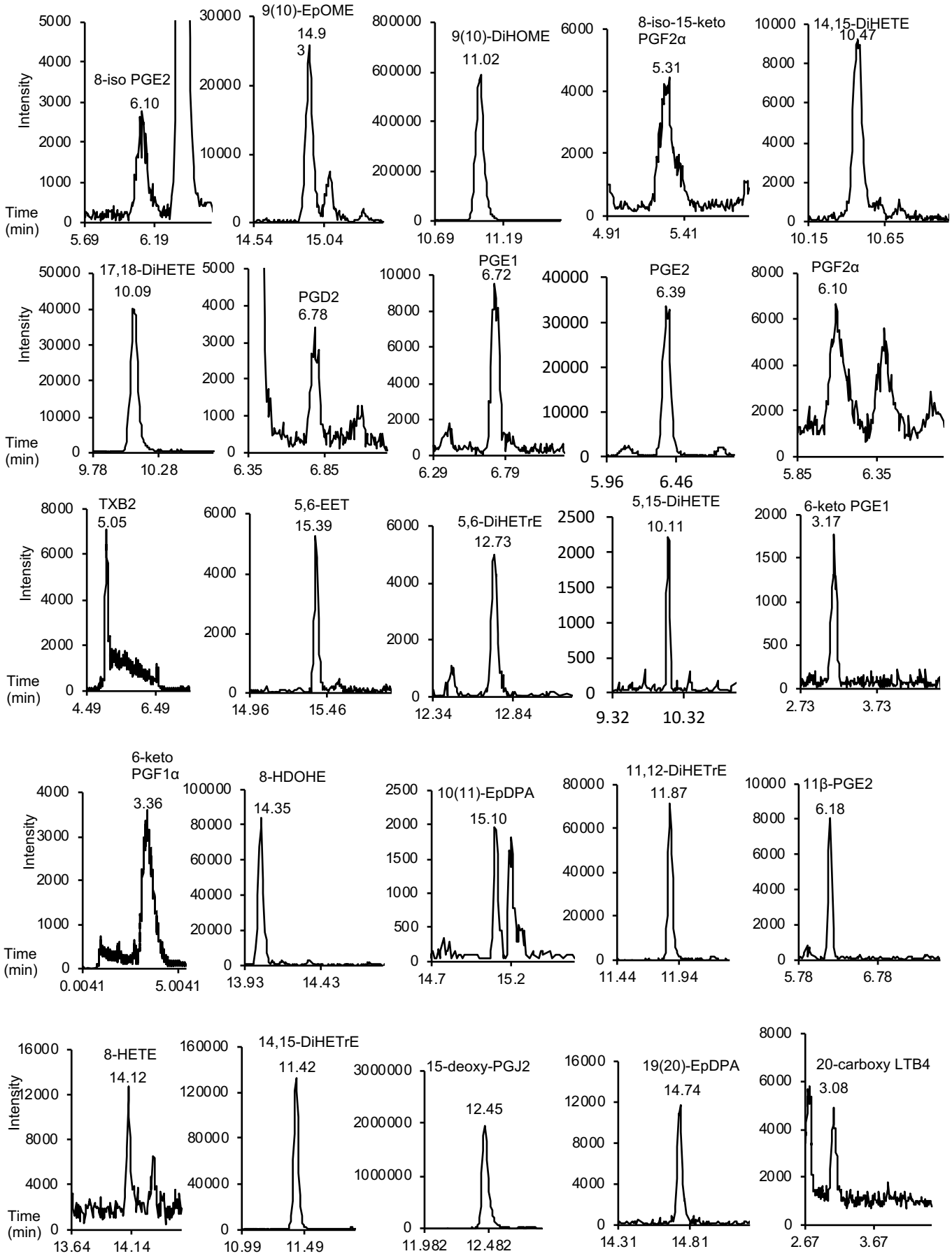
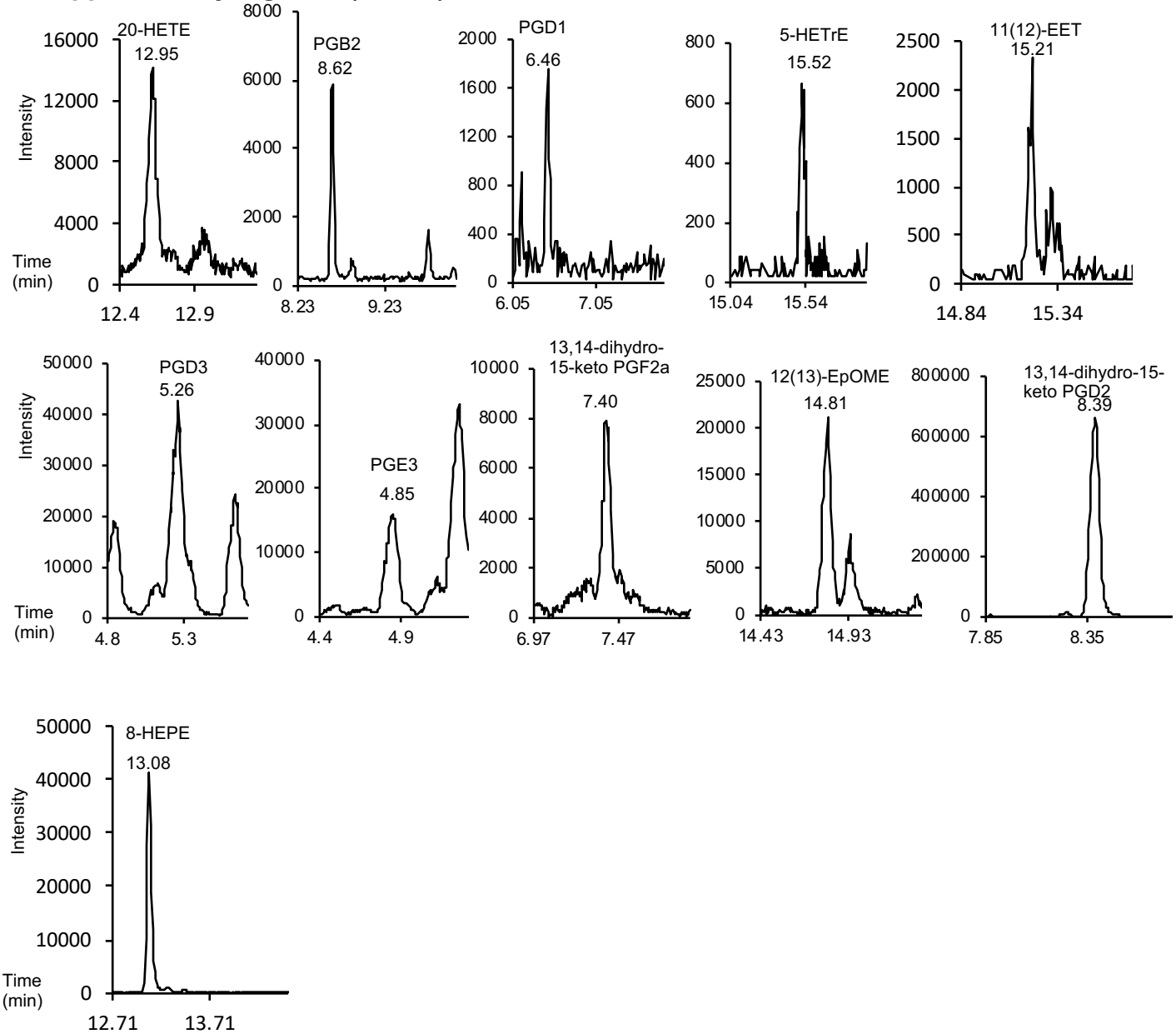
Supplementary Figure 7 (contd.)